Airborne laser swath mapping of the summit of Erebus volcano, Antarctica: Applications to geological mapping of a volcano

Bea Csatho[a,1], Toni Schenk[b], Philip Kyle[c], Terry Wilson[d], William B. Krabill[e]

[a]Department of Geology, University at Buffalo, 855 Natural Sciences Complex, Buffalo, NY 14260, USA, bcsatho@buffalo.edu

[b]Department of Civil and Environmental Engineering and Geodetic Science, 2070 Neil Av., The Ohio State University, Columbus, OH 43210, USA, schenk.2@osu.edu

[c]Department of Earth & Environmental Science, New Mexico Institute of Mining and Technology, Socorro NM 87801, USA, kyle@nmt.edu

[d]School of Earth Sciences, 125 S. Oval Mall, The Ohio State University, Columbus, OH 43210, USA, wilson.43@osu.edu

[e]Cryospheric Sciences Branch NASA/GSFC/Wallops Flight Facility Wallops Island, VA, USA, 23337, USA, william.b.krabill@nasa.gov

[1]Corresponding author:
Department of Geology, University at Buffalo,
855 Natural Sciences Complex, Buffalo, NY 14260-3050, USA
E-mail: bcsatho@buffalo.edu
Phone: 716-645-6800 x3921
Fax: 716-645-3999

In Press, Special Issue on Erebus Volcano, Journal of Volcanology and Geothermal Research

Keywords: Erebus volcano, lidar, volcanic geomorphology, DEM generation, feature extraction

Abstract

The lidar observations reported here have provided the first high precision topographic data on the active craters of Erebus volcano, Antarctica. Digital elevation data are invaluable for geomorphic analysis of volcanoes especially when combined with methods to automatically extract landscape features. The data are indispensable for studying eruptive events and volcano-tectonic processes. Airborne laser scanning or lidar is a rapidly emerging technology to map surface topography with high accuracy and detail, comparable to a 1:1 000 scale map. In the austral summer of 2001-2002 airborne laser scanning data were collected in Antarctica over the summit plateau of Erebus volcano. We describe the high-resolution data set from Erebus, products derived from the data and demonstrate how extracted topographic features can be used in the geomorphic analysis of volcanoes. Background is presented on the airborne laser scanning method and on the accuracy estimation of laser points. We describe the computation of a high-resolution DEM with a grid size of 2 m x 2 m for the summit area of Erebus volcano. Errors in the DEM are assessed using independent ground-based GPS data and the RMS error is estimated to be ±0.39 m. Visualization methods reveal topographic features that are very useful for geomorphic analysis. Automatic feature extraction and processing is necessary to exploit the high-resolution and accurate elevation data. Methods are described to extract 1D and 2D features and organize them for subsequent analysis. Fitting analytical functions to 3D point clouds or DEMs is particularly effective in extracting topographic features, including planes, higher order surfaces, cones, and conic sections. These methods are used to obtain a quantitative description of the calderas and modern-day crater of Erebus. Especially valuable are the measured surface areas if the lava lakes as this controls thermal emissions and gas fluxes from the volcano. Examination of the surface elevations of Ray Lava Lake, Werner Vent and Active Vent indicates that the active vents were more or less in magmastatic equilibrium in 2001 December. Conic segments are fitted to mapped sections of caldera rims to identify the sections buried under younger lava flows or covered by ice and snow. Automatic methods are used to detect and characterize lava channels using geomorphometric maps generated from the DEM.

1. Introduction

Geomorphology provides fundamental information about the structure and evolution of volcanoes (Cotton, 1944; Thouret, 1999). Landscape features record eruptive events and processes, aspects of the erupted materials, and bear signatures of deformations associated with volcanic and volcano-tectonic processes. The geomorphic analysis of volcanoes greatly benefits from digital elevation data, and processing methods to enhance or extract landscape features is rapidly becoming an indispensable tool (e.g., Favalli et al., 1999; Adiyaman et al., 1998; Hubbard et al., 2007; Kervyn et al., 2007). Remote sensing is ideal for collecting data in vast, remote and inhospitable regions such as Antarctica. Until recently, however, the resolution of images and topographic data has been insufficient for many geological mapping applications.

Airborne Laser Scanning (ALS), also referred to as LIght Detection And Ranging (lidar) mapping, uses laser ranging from aircraft platforms to map surface topography with high accuracy and details, comparable to 1:1 000 map scales (Carter et al., 2001; Csatho et al., 2005). High-resolution topographic data from ALS proves to be particularly effective for mapping geomorphic features formed by glacial and active tectonic processes (Haugerud et al., 2003; Cunningham et al., 2006). Lidar data are becoming more widely used in volcanology, for example to map basaltic lava channels on Mount Etna (Mazzarini et al., 2005; 2007), to examine gravity flows associated with the 1944 eruption of Vesuvius (Ventura and Vilardo, 2008), to conduct morphometric analysis of the Amboy Crater volcanic flow in the Mojave Desert (Finnegan et al., 2004), to delineate flow units and rootless cones in Nova Scotia (Webster et al., 2006), and to characterize pyroclastic and lava flows in Costa Rica (Hofton at al., 2006).

Until recently the only topographic maps available for Mt. Erebus were a 1:250 000 map of the U.S. Geological Survey (USGS) with 200 m contour intervals, and a large scale map of the summit area, compiled in 1970 from aerial photographs. This latter map covers much of the same area as the lidar Digital Elevation Model (DEM) discussed here. Recently the U.S. Geological Survey (USGS) and the Land Information New Zealand (LINZ) produced a 1:50 000 digital topographic map of the entire Ross Island with 20 m contour intervals by using photogrammetric methods. Satellite remote sensing studies of

Erebus to date have focused on monitoring the thermal anomalies of the active lava lake (Rothery and Oppenheimer, 1994; Davies et al., 2008; Wright and Pilger, 2008).

In the austral summer of 2001-2002, NASA's Airborne Topographic Mapper (ATM) system was deployed to Antarctica under the auspices of NASA, NSF and the USGS. ALS data were collected over the summit plateau of Erebus volcano and several sites in the McMurdo Sound region (Csatho et al., 2005). This paper examines the new high-resolution ALS data set and its derived products for the summit area of Erebus volcano. We describe the generation and accuracy assessment of the high-resolution DEM and present a series of 2D and 3D visualizations with corresponding profiles, highlighting the ways in which the new topographic data can be applied for geomorphic and geologic analysis of a volcano. We also introduce topographic feature extraction methods and show how they can be applied to map caldera rims, craters and lava flows, for example.

2. Background

2.1. Erebus volcano

Mount Erebus, the world's southernmost active volcano, is a intraplate alkaline stratovolcano located within the West Antarctic rift system (Behrendt, 1999). Its volume of ~2 000 km^3 makes it one of the larger volcanoes in the world. It belongs to the McMurdo Volcanic Group, which is an extensive alkali volcanic province, comparable to the East African rift system (Kyle, 1990a, Kyle et al., 1992). Erebus volcano is young, being built entirely within the last 1.3 Ma (Esser et al., 2004), and its summit cone has formed over the last few thousand years. Since regular observations began in the early 1970's, there has been a persistent convecting anorthoclase phonolite lava lake within the summit crater and daily Strombolian eruptions occur (Kyle et al., 1982; Aster et al., 2004).

Mount Erebus is the largest volcano of the Ross Island, surrounded by Mount Bird in the north, Mount Terror to the east and a narrow, long line of vents extending along the Hut Point Peninsula to the Observation Hill near McMurdo Station (Fig. 1). Because it is a young, undissected volcano, there is only limited access to sample sites to study the older deposits that record its early development. Instead,

stratigraphy has been combined with topographic data to reconstruct the evolution of Mount Erebus (Esser et al., 2004; Harpel et al., 2004).

2.2. Principle of airborne laser scanning (ALS)

Overviews of the ALS methodology is given by Wehr and Lohr (1999). Here we give details on the procedures we used to generate a high resolution DEM of the summit area of Erebus volcano. Fig. 2 illustrates the principle of airborne laser mapping. In general, a laser point, **p** is obtained by:

$$\mathbf{p} = \mathbf{g} + \mathbf{r} \tag{1}$$

where **g** is the aircraft position and **r** the range vector. Differential carrier phase GPS processing provides the aircraft position (phase center of the GPS antenna attached to the fuselage). The magnitude of the range vector, referred to as "the range", is calculated from the travel time of the laser pulse between the laser system, reflective surface, and back. The scan angle, recorded by the laser scanning system and the aircraft attitude, measured by an Inertial Navigation System (INS), determine the direction of the range vector. To facilitate the computation of the laser points, both the position and the attitude of the aircraft must be in the same reference system. We used the World Geodetic System 1984, known as WGS-84, because GPS positions are processed in this well defined, earth-centered reference frame.

While the principle of airborne laser mapping is very simple, a number of intricate details complicate matters and ultimately determine the quality of the laser points. The GPS antenna, the INS unit, and the laser scanning system are physically separated. Their precise relationship must be determined by calibration procedures (e.g., Krabill et al., 2002). Although the oscillators used to measure the travel time of the laser pulse are accurate (e.g. 0.1 ns, resulting in a range accuracy of 1.5 cm), the returning laser energy that is reflected from a small area (e.g., 0.5-1 m), called a footprint, is miniscule. The surface topography and roughness within the footprint deform the returning pulse, making an exact comparison of emitted and returned laser pulse a challenge.

In order to obtain area coverage, the laser beam is deflected by a mirror. Most commercial laser

scanning systems employ a linear scanner with the rotation axis located within the mirror plane. In contrast, NASA's ATM system uses a conical scanning system. Here, the mirror rotates about an axis that is at an angle to the mirror surface (nutating mirror), causing an egg-shape scan pattern. With an off-nadir angle of 15^{o}, scan frequency of 20 Hz, pulse rate of 5000 Hz, and a flying height of 500 m, the swath width is 268 m, and the maximum laser point spacing across the flight direction is about 3.4 m. Obviously, the spacing of the conical scan patterns along trajectories depends solely on the aircraft speed (e.g., a velocity of 60 ms^{-1} and a scan frequency of 20 Hz gives a data spacing of 3 m). The numbers used in this example are typical for the ATM mission on Erebus. The surface topography and roughness within the footprint deform the returning pulse, making the exact measurement of the travel time a challenge. NASA's ATM system solves this problem by measuring the energy of the returning pulse until a threshold is reached which determines the time and hence the range. This simple single range method works well as long as the surface within the footprint is rather smooth and void of vegetation.

Figure 3 shows the location of the laser points of two consecutive scans from one of the missions on Erebus volcano. The number of points per scan is given by the ratio of pulse rate to scan rate (e.g., 5000/20=250 points). Fig. 3 depicts the egg-shape scan pattern and the irregular point distribution, which is very dense at the swath boundaries and least dense in the center. We also recognize missing points, either not processed due to low returning laser pulse energy, or removed by blunder detection (explained in Sec. 3.1).

2.3. Computation of laser points

From the recorded measurements of range, scan angle, and GPS/INS data, the latitude, longitude, and elevation of the laser footprint is computed for each laser pulse. Processing begins with a careful determination of calibration parameters pertaining to the GPS, INS, and laser scanning system (Krabill et al., 2002). All these system components are affected by various systematic errors, some of which are even changing during data acquisition. The quality (precision, reliability) of the computed laser points depends a great deal on how well systematic errors (system biases) have been removed.

After calibrating the measurements and removing system biases, the computation of laser point positions is straightforward. The position of the laser's firing point at the time of emitting a laser pulse is interpolated from the GPS antenna positions that are recorded regularly at one second time intervals. This requires exact time synchronization of laser pulse firing with the GPS clock. In a similar fashion, the orientation of the laser beam is interpolated from the INS attitude parameters, recorded at the 256 Hz sampling frequency of the INS system.

2.4. Accuracy of laser points

Derivation of the laser point accuracy starts with Eq. 1. We note that a laser point is determined by measurements of the laser scanning system (here scan angle and range) and the navigation system (GPS/INS). While a random GPS error directly propagates to a laser point, random INS errors (attitude errors) propagate linearly as a function of the range. The same is true for the angular error of the laser scanning system. Lumping the attitude and scan angle errors together to a random directional error, σ_d, and considering Fig. 4a, we have

$$\Delta s \approx r \cdot \sigma_d \tag{2}$$

$$\Delta p_d = \Delta s \cos\alpha = \sigma_d H \tag{3}$$

$$\Delta z_d = \Delta s \sin\alpha = \sigma_d H \tan\alpha \tag{4}$$

where α is the off-nadir (conical) angle, r the range, Δp_d the horizontal (planimetric) error and Δz_d the elevation error. Fig. 4b shows the impact of a range error. Its horizontal and vertical components are:

$$\Delta p_r = \sigma_r \sin\alpha \qquad \Delta z_r = \sigma_r \cos\alpha \tag{5}$$

It should be noted that the range error is independent of the range or the flying height, in contrast to the directional error. Finally, a random GPS error, σ_{GPS}, with a horizontal and vertical component of σ^p_{GPS} and σ^z_{GPS}, respectively, propagates directly to the laser point error as shown below

$$\Delta p_g = \sigma^p_{GPS} \qquad \Delta z_g = \sigma^z_{GPS}\,. \tag{6}$$

These three error sources determine the laser point error as follows

$$\Delta p = (\Delta p_d^2 + \Delta p_r^2 + \Delta p_g^2)^{1/2} \tag{7}$$

$$\Delta z = (\Delta z_d^2 + \Delta z_r^2 + \Delta z_g^2)^{1/2}\,. \tag{8}$$

The following example with realistic assumptions about errors provides a sense of the magnitude of laser point errors. Assume a flying height of 500 m, off-nadir angle of $\alpha = 15°$, and random errors of $\sigma_d = \pm 0.05°$, $\sigma_r = \pm 0.01\,\text{m}$, $\sigma^p_{GPS} = \pm 0.1\,\text{m}$ and $\sigma^z_{GPS} = \pm 0.15\,\text{m}$. This will result in a horizontal error of $\Delta p = \pm 0.43\,\text{m}$ and a vertical error of $\Delta z = \pm 0.15\,\text{m}$. The example confirms the practical experience that, (i) horizontal errors are larger than elevation errors, and (ii) the GPS elevation error, σ^z_{GPS}, is the primary source for the laser point elevation error—at least for near horizontal surfaces. For hilly areas, such as the steep slopes of volcanoes, the horizontal error causes an additional elevation error, however. Fig. 4c illustrates this scenario from which we readily obtain the additional elevation error, $\Delta z'$, as

$$\Delta z' = \Delta p \tan\gamma \tag{9}$$

With the previous example but now taking into account a slope of $\gamma = 20°$, this additional elevation error is $\Delta z' = \pm 0.16\,\text{m}$. It exceeds the primary elevation error and increases the total elevation error to $\pm\, 0.21\,\text{m}$.

3. High-resolution DEM of the summit area of Erebus volcano

This section describes how the DEM was generated from laser points acquired by the airborne laser scanning system; it is referred to as ALS DEM. Fig. 5 shows the aircraft trajectories flown over the summit plateau of Mount Erebus.

3.1. Blunder detection

Prior to the DEM computation, blunders must be detected and removed from the laser point cloud.

The classical measurement theory introduces three types of errors associated to observations: (i) random errors are inevitable, are always present and thus an observation is considered a random variable; (ii) systematic errors, caused by imperfect instruments; (iii) blunders (or outliers), usually associated to (human) mistakes when reading or recording the value of an observation. In automatic measuring systems, such as airborne laser scanning, it is not obvious why a measurement would occasionally be wrong because the overwhelming majority of instrument imperfections are systematic errors. Thus we need to elaborate the notion of blunders a bit further. We also note that the computation of laser points has no inherent redundancy because there is no additional information in the measurements that could be used to check the points. For example, a wrong range will lead to a wrong laser point, without warning. We can easily relate random and systematic errors to the range but what is a blunder? Suppose the laser pulse is reflected from an object above the Earth's surface, say a cloud. Consequently, the laser point will be 'wrong' with respect to points on the ground. But let us now consider the frequently occurring situation in the Dry Valleys of Antarctica where some laser points happen to be on the top or on the side of boulders. This will cause a problem for creating DEMs but it might be very desirable for someone interested in studying the size and distribution of boulders, for example. We realize that the notion of blunders is application dependent. Moreover, blunders may be small and difficult to detect.

Blunder detection is performed at three stages: prior, during, and after the DEM generation. The following is a brief description of the first stage. Blunder detection during and after DEM generation will be described in the next section. The processed ATM data sets from NASA are time-sequentially organized, scan after scan. This suggests analyzing the laser points within a scan because consecutive points must be close to each other. Let us assume for a moment that the laser points of one scan are on a planar surface. Then, the points form the ideal egg-shape scan pattern discussed in Sec. 2.2. Suppose now that one of the laser points is above the plane. Since its range will be shorter, the point will lie inside the scan pattern, displaced radially from its ideal scan pattern position. In reality, the points of a scan are on a more complex surface, causing deviations from the ideal scan pattern. However, blunders still show up as

distinct displacements from a piecewise smooth scan pattern and can be detected accordingly as Fig. 3 illustrates. This simple blunder detection scheme is very effective and resulted in the removal of about 98% of all blunders.

3.2. DEM generation

The generation of a DEM amounts to determining elevations at regularly spaced grid locations (grid posts) from the neighboring, irregularly distributed laser points. First, a suitable grid-spacing must be selected. Apart from application-driven considerations, the minimum size should be chosen such that a grid cell contains at least one laser point. With a point density of 0.25 points/m^2 for Erebus we obtain the desired grid size of 2 m × 2 m.

DEM elevations refer to the Earth's surface, stripped from objects that are smaller than the grid size and whose vertical dimension exceeds three times the anticipated laser point accuracy. This surface is also called *bare earth* or *topographic surface*. Since the laser points are calculated with respect to the WGS-84 ellipsoid, the elevations are ellipsoidal heights. This is in contrast to older topographic maps, which usually show orthometric heights. Fig. 6 illustrates the relationship between ellipsoidal and orthometric heights. The latter refers to the geoid – an equipotential surface that approximates mean sea level. Hence orthometric heights are sometimes informally called *elevations above sea level*. The height differences ellipsoid/geoid are known as geoid undulations, denoted by **Error! Objects cannot be created from editing field codes.** in Fig. 6. The conversion of ellipsoidal to orthometric heights (or vice versa) can be readily performed with open domain software (e.g., geoid height calculator at http://sps.unavco.org/geoid/). The geoid undulations in the vicinity of Erebus are nearly constant (between -53.68 m and -53.85 m). For all practical purposes the geoid can be considered parallel to the ellipsoid in this region and the relationship between ellipsoidal/orthometric heights is simply given by:

$$h_e = h_o - u \tag{10}$$

with h_0 the orthometric height, h_e the WGS-84 ellipsoidal height, and u the geoid undulation (-53.76 m), estimated by the EGM96 model (Lemoine et al., 1998). In conclusion, orthometric heights are about 54 m

higher than ellipsoidal heights. From the ALS data we can readily determine the highest point of Mount Erebus: 3739.45 m. By adding the geoid undulation we obtain an orthometric height of 3793.21 m. This compares well with the widely published number of 3794 m as the height of Mount Erebus.

The computation of elevations at known grid locations is a slightly modified version of what we have described in Csatho et al. (2001). It comprises the following steps:

(i) select laser points around a grid post;

(ii) fit a planar or second order surface through the selected points;

(iii) compute the elevation on the fitted surface at the grid location;

(iv) determine the quality of the interpolated elevation and label it accordingly;

(v) after all grid posts have been processed with steps (i) – (iv), perform an overall quality control of the entire DEM.

The Erebus DEM is about 9 km × 10 km, contains 11.7 million laser points and 11.1 million valid grid posts where elevation could be interpolated. These numbers make clear that good data structures and efficient algorithms are essential. A frequently occurring task is to extract all points within a region of interest, for example by specifying a geographic location and a search radius. To expedite such queries we used *Oracle Spatial* database to store and access the points.

The first step in the DEM processing scheme requires the extraction of laser points around a grid post. The grid post defines the center of the area to be searched for laser points. The search area's size and shape is determined adaptively, based on the number of points (a few points more than needed for the surface fitting process) and their distribution. As a rule, the grid post must be inside the convex hull of the extracted points to avoid that the elevation will become the result of *extrapolation* with its notorious bad error propagation. The next step is concerned with fitting a surface through the extracted laser points. The following mathematical model was used:

$$z = a_1 \cdot x^2 + a_2 \cdot y^2 + a_3 \cdot x \cdot y + a_4 \cdot x + a_5 \cdot y + a_6 \qquad (11)$$

The unknown coefficients $a_1, \ldots, a_6$ are determined by a robust estimation because the initial blunder

detection phase may not have removed all points that are not on the topographic surface. Specifically, we use the Least Median of Squares (LmedS) estimator that is known to be immune to as many as 50% blunders (Köster and Spann, 2000).

After surface fitting, an elevation is computed at the grid location with Eq. 11. The quality control is based on rigorous error propagation, taking into account the fitting error, the variance-covariance matrix of the fitting process, and—more importantly—the location of the grid post relative to the laser points used to fit the surface. Note that the elevation error is different for every point on the surface. The accuracy of an interpolated point decreases the further the point is from the centroid of the laser points. Based on this, labels are assigned to every grid post, essentially quantifying the accuracy and reliability of the DEM elevations. Labels are discussed in detail in Schenk et al. (2004).

After all grid points are processed, the DEM is analyzed by different visualization methods. Although human inspection is subjective, this last quality control measure is quite effective because the human visual system is very sensitive to artifacts, that is, to surfaces that do not 'look right'.

Fig. 7 is a color shaded relief rendition of the DEM and the slope map calculated from it is shown in Fig. 8. Readers interested in obtaining the DEM can download it from the United States Antarctic Resource Center (USARC, *http://usarc.usgs.gov/lidar_dload.shtml*) and a shaded relief version of the DEM displayed in Google Earth is available from *http://rsl.geology.buffalo.edu/dryvalleys_dem.html*

In addition to the high-resolution ALS DEM we also created a DEM covering the entire Ross Island by fusing the ALS DEM with elevation data from the 1:50 000 digital topographic map generated by USGS and the Land Information New Zealand (LINZ). In order to be compatible with the ALS DEM we transformed the map data to WGS-84 which essentially is a conversion of the orthometric map elevations to ellipsoidal heights. The Ross Island DEM, shown in Fig. 1, has a grid spacing of 20 m, an elevation accuracy of ±6 m, covers an area of 74 km × 74 km, and the grid posts over the summit area coincide with that of the ALS DEM. The Ross Island DEM is used to create the 3D visualization and the slope map of the entire Mt. Erebus, as shown in Fig. 9.

3.3. Accuracy assessment

In this section we present a brief analysis of the DEM accuracy. It is assumed that blunders and systematic errors have been removed and only random measurement errors are present. By and large, the elevation accuracy of a DEM (grid) point is affected by:

(i) accuracy of laser points in the vicinity of a DEM point;

(ii) distribution and density of laser points in the vicinity of a DEM point;

(iii) interpolation method used to determine DEM points;

(iv) surface roughness in the vicinity of a DEM point.

The interconnection of these factors and their spatial variability means that the theoretically correct derivation of the accuracy of a DEM point from the original measurements is complex. We follow a more qualitative approach in this paper, however, and start the discussion by referring to Fig. 10. Here, the topographic surface is shown as a solid line. Open circles represent laser points and solid circles are DEM grid points. The fitted surface, shown as dashed line, is obtained by fitting an analytical surface through laser points (Sec. 3.2.). The DEM points are on the fitted surface and we call the difference between fitted and topographic surface the DEM error, denoted by *d* in Fig. 10. The following discussion focuses on the main factors that contribute to this error. Recall that the fitted surface is a 2D analytical function (Eq. 11), the coefficients of which are obtained by minimizing the differences to the laser points in a least squares sense. This difference, called fitting error is denoted by *f* in Fig. 10. The least-squares approach offers two significant advantages. For one it is simple to implement. Moreover the adjustment procedure does not only find the best estimates of the surface coefficients but also their accuracies. That is, we have a clear error budget for every fitted surface and it is straightforward to derive the accuracy of any point on the fitted surface by error propagation. For example for a planar surface, represented by, $z = a \cdot x + b \cdot y + c$ we have

$$\sigma_z = \left(\sigma_a^2 x^2 + \sigma_b^2 y^2 + \sigma_c^2\right)^{1/2} \tag{12}$$

where $\sigma_a, \sigma_b, \sigma_c$ are the standard deviations of the plane coefficients *a*, *b*, *c* and *x*, *y* are the coordinates

of the DEM grid post. Eq. 12 makes clear that the accuracy of a point on the fitted surface changes as a function of its location.

To further examine the DEM accuracy we take a closer look at Eq. 12 and note that the standard deviations of the polynomial coefficients of the fitting surface depend on the distribution of the laser points and their accuracy. The laser point accuracy, discussed in Sec. 2.4., is shown in Fig. 10 as the difference between the topographic surface and the actual laser point, labeled *e*. There is yet another source contributing to the fitted surface error, called modeling error here. Suppose a specific topographic surface has the shape of a second order polynomial but for some reason we chose a plane as the fitting surface (e.g. too few laser points to fit higher order surface). This will introduce an error because a wrong mathematical model (plane) is used to describe the physical reality (2^{nd} order surface).

Finally, we address the last error source—the sampling error. Examining Fig. 10 closely reveals that the topographic surface has many more details as can possibly be captured by the laser points. For example, most of the surface details between the left most and next laser point will be lost. We conclude that the error between the topographic surface and the fitted surface is not only a function of the laser point accuracy but also depends on the sampling density with respect to the surface characteristic. Obviously, this is a scale problem and thus application dependent. It follows that the DEM for Erebus with a grid spacing of 2 m × 2 m and a laser density of 0.25 point/m^2 cannot capture morphological details of sub-meter dimensions.

3.4. Accuracy assessment with GPS observations

To assess the theoretical estimates of the DEM accuracy discussed in Sec. 2.4., we performed checks relying on GPS observations made in the summit area of Erebus volcano (Fig. 7). GPS data were collected at several locations as part of the Erebus deformation network (Kyle et al., 2001; Bartel et al., 2003; Aster et al., 2004) and the Trans-Antarctic Mountains DEFormation Network (TAMDEF) project (Willis et al., 2006).

We have identified 13 GPS stations with dual frequency GPS observations, acquired by geodetic

GPS receivers during the last 10 years, either as continuous (several months or more at each time) or campaign observations (1-7 days, repeated in several years). Precise elevations of these checkpoints were calculated by differential carrier phase processing. All GPS observations are from the time period 1997-2004 during which vertical crustal and volcanic deformations are in the order of a few cm, much smaller than the expected error of the ALS DEM.

Table 1 contains the results of the accuracy assessment, including the GPS station identification, the position and elevation of the checkpoints, and the corresponding DEM elevations, obtained by a bi-linear interpolation from four neighboring DEM grid points. The fifth column contains the difference between GPS checkpoint and interpolated DEM elevation. Station EAST (third entry in Table 1) is located close to the edge of a vertical cliff, about 2 m high. We excluded this station from the statistical analysis because a small horizontal error may result in a large elevation error. The root-mean-square error (RMS) calculation of the remaining 12 checkpoints resulted in 0.32 m (mean) and ±0.39 m (standard deviation). The major factor contributing to the mean (bias) of 0.32 m is the fact that GPS monuments are often established on the top of small ridges to obtain unobstructed sky-view for the observations. The laser point density and the derived DEM don't capture the topographic details of these small ridges and thus they cause a bias in elevation. The standard deviation of the elevation difference contains the random GPS and DEM elevation errors. Considering a random GPS elevation error of ±0.15 m we obtain σ_{DEM} = ±0.35 m for the random DEM elevation error. This error is larger than the theoretical estimate given in the previous section. One plausible explanation is that the horizontal DEM error is larger than assumed in the theoretical error model, causing a considerable secondary elevation error (see Fig. 4c). This explanation is supported by a similar checkpoint computation performed in flat areas of the McMurdo Dry Valleys where we obtained an RMS error of ±0.2 m between GPS and DEM elevations using 19 checkpoints on slopes less then 5 degrees (Csatho et al., 2005).

3.5. Postprocessing and visualization of ALS DEM and image products

Traditional representation methods and processing tools lack the ability to present and extract the rich

spatial information of high-resolution DEMs. New visualization and feature extraction methods, such as those presented in this and in the following sections, are needed to assist experts in their interpretation and analysis of topographic features and landforms of volcanoes. For example, by visualizing DEMs as shaded relief images subtle topographic features can be recognized, or crosscutting relationship of fissures, cones and faults can be interpreted. Accurate, high-resolution DEMs are ideal for geomorphometric analysis and for extracting geomorphological features, enabling quantitative analysis of landforms.

In this section we illustrate the different data sets obtained from the ALS survey. We examine a small area on the NW flank of Erebus volcano (Fig. 11, highlighted in Fig. 7). Fig. 11a presents a traditional color representation of the DEM. Fig.11b illustrates how small details become visible by combining the color DEM with a shaded relief representation. Shaded relief visualization also enhances the random noise of the DEM. To reduce this undesirable effect, the DEM was smoothed prior to visualization. The Lee filter (Lee, 1980), which is based on statistics calculated in a moving window, is very effective for this purpose. Unlike typical low-pass smoothing filters, it preserves image sharpness and details while suppressing noise. The slope map (Fig 11c) is derived from the original ALS DEM by computing the surface gradient within a 3**Error! Objects cannot be created from editing field codes.**3 (6 m × 6 m) window.

Fig. 11d shows a morphometric map derived from the DEM by using ENVI (ITT Industries, Inc.). Geomorphometry (quantitative study of landforms) has been successfully applied for mapping glacial and periglacial landforms from ALS DEMs in the McMurdo Dry Valleys (Dora, 2005). Geomorphometric analysis usually starts with computing topographic elements, such as slope, aspect, plan and profile curvatures from a DEM. Polynomial surface fitting is widely used for computing these primary attributes. It fits a quadratic surface to the digital elevation data and calculates the slope and curvature of this fitted surface (Wood, 1996). The primary attributes are then used for classifying the terrain types at each grid post into different categories, including peaks, ridges, passes, planes, channels or pits. For example, a sloping surface that is concave in the cross-sectional direction will be classified as a channel. In contrast, a convex sloping surface is a ridge. Surface patches that can be approximated by planar surfaces are

classified as planes. The morphometric map shows planar surfaces in light green color, while dark blue color marks ridges, corresponding to lava levees. Most pixels with ocher color indicate lava channels, but they also occur within the elongated depressions between neighboring lava flows. As shown in Sec. 5.3.2., this morphometric classification map is a suitable input for the feature extraction process, for example for mapping lava flows.

In addition to the laser point coordinates, used as input for the DEM generation, ATM data include the back-scattered laser energy and the reflected solar radiation for each laser footprint. The back-scattered laser energy, usually called intensity, is a function of the material properties and the surface geometry within the laser footprint (e.g., reflectance, slope, surface roughness). The ability to record reflected solar radiation between consecutive laser shots is a unique feature of the ATM system. This "passive mode" emulates a camera, except that the ground is not contiguously covered. To visualize the reflected laser energy (intensity) and reflected solar radiation, images are created by interpolating the irregularly distributed footprints into a regular grid. Since the resulting images are derived from ATM data they, too, are registered to the WGS-84 system. That is, the intensity image and the solar radiation image are orthophotos. These images provide information about the composition and physical conditions of the surface, enabling users to delineate different lithologic units, snow cover, or estimate the age of different lava flows (Mazzarini et al., 2007). Fig. 11e shows the solar radiation image. Changes in grey levels are caused by topography and changes in surface reflectivity. Thus the appearance is similar to an aerial photograph as the comparison of the solar radiation image and an aerial photograph (Fig. 11f) demonstrates.

4. Geologic and geomorphic mapping of Erebus volcano

4.1. Growth phases, volcanic alignment and structure

The evolution of Erebus volcano has been reconstructed using recent geochronology studies (Esser et al., 2004; Harpel et al., 2004; Kelly et al., 2008). The excessive snow and ice cover hampers reconstruction of its eruptive history (Moore and Kyle, 1987, 1990). Therefore topographic data provide

key information for reconstructing the phases of volcano development. We use the new DEMs and elevation profiles extracted from them to illustrate the evolution of Erebus and highlight previously unrecognized volcanic and structural elements.

The main phases of the volcano evolution are explained with the help of a NE-SW elevation profile extracted from the Ross Island DEM (Fig. 12). The gentle slopes of the lower volcano (slopes $\leq 10^{o}$), exposed below 1500 m elevation (Fig. 9b), are associated with a proto-Erebus shield phase of growth by effusion of low viscosity lava. The steeper, upper slopes record a second phase of cone building characterized by higher-viscosity, anorthoclase-phyric tephriphonolite lavas that dominate all surface exposures on the volcano. This second, proto-Erebus cone building phase started around 1 Ma ago and ended 250 ka ago. The collapse of the proto-Erebus cone about 700 ka ago created the Fang Ridge escarpment, which today is manifested by Fang Ridge, a prominent NW-SE-striking ridge at ~3000 - 3100 m elevation (Figs. 7 and 9a).

The third, modern-Erebus cone building phase, which started 250 ka ago, is characterized by anorthoclase-phyric tephriphonolite lava from summit and flank vents (Harpel et al., 2004). According to Harpel et al. (2004) and Kelly et al. (2008) at least two caldera-collapse events occurred during this period. The geologic map of the summit area in Fig. 13a, reproduced from Harper et al., (2004), shows the pre-caldera lava flows associated with the older and younger caldera collapse events, the post-caldera lava flows and vents on the summit plateau as well as locations of samples dated by the $^{40}Ar/^{39}Ar$ dating method. The older caldera collapse event, indicated by a change in surface slope at about 3150 - 3450 m, (Fig. 12) likely occurred between ~ 90 to 70 ka. It is constrained by the youngest pre-collapse summit flow (87±7 ka) and the oldest post-collapse summit flow (76±5 ka). A superimposed younger modern-Erebus caldera-collapse event that occurred between 25 and 11 ka created the nested pre-caldera rim in the SW corner of the summit plateau. This caldera rim is composed of pre-caldera flows dated 21±4 and 27±3 ka. The calderas are filled with lava younger than 17 ka.

The ALS DEM covers the upper flanks and the summit plateau of Erebus, above 2500 m elevation (Fig. 7). It depicts the circular shape of the Mount Erebus summit plateau as well as the modern

summit cone complex (elevation ≥ 3400 m), which is elongated in ENE direction, and placed asymmetrically toward SW on the summit plateau. The caldera collapse events are indicated by changes in slope with steep slopes below the caldera rims (Figs. 8 and 12). A linear feature, crossing the summit plateau and aligned with the main elongation of the modern summit cone complex, is clearly visible on the slope map (Fig. 8, large arrow). This feature, called Ice Tower Ridge, trending at N60^{o}E and corresponding to a linear alignment of vents is marked by fumarole towers, craters and collapse features on the ice surface and was interpreted as a rift system (Otway et al., 1994). Several other linear alignments can be identified on the slope map, for example in E16^{o}S, E44^{o}S and N24^{o}E directions (Fig. 8, small arrows). These alignments indicate possible rift systems and structural control on volcanic activity.

The new DEMs also allow us to improve the volume estimates of Erebus volcano. From the Ross Island DEM the total surface area of Mount Erebus, including Hut Point Peninsula, is 1053 km^2 and its total volume above sea level is 1096 km^3. The estimated volume of the Erebus volcano summit cone (above 3400 m elevation) is 1.12 km^3. Esser et al., (2004) estimated the average eruption rate of the modern-Erebus to be approximately 4.0 km^3/ka, over its 250 ka time-span. This indicates that the modern-day summit cone has been built within a relatively short time, possibly less than a thousand years.

4.2. Volcanic and structural geomorphology

We rely on the geologic map of the summit plateau (Fig. 13a), stereo aerial photographs, and a draft geomorphology map (Kyle et al., 1982) to assess the potential of the ALS DEM for geomorphologic mapping.

Figs. 13b and c show 3D visualizations of geologic information by draping the geologic map on the ALS DEM. This type of presentation of fused thematic and topographic information facilitates the reconstruction of the caldera rims (Fig. 13b) and supports the mapping of the distribution, morphologies, orientation and crosscutting relationship of lava flows, faults and other geomorphological features (Fig. 13c).

The shaded relief representation of the ALS DEM (Fig. 14a) vividly depicts the volcanic landforms of the summit plateau and reveals the complex structure of the crater. Lava channels are easily recognizable because of their parallel levees. A prominent example is the pair of well-developed levees of the Tramway Ridge Flow, located on the steepest, NW part of the summit plateau. The surface of the summit plateau is smooth with the exception of its northern region, which is covered by short, discontinuous lava ridges (Fig. 14a). In contrast, the steeper flanks of Erebus are covered with well-developed lava channels. This fact confirms that the development of the lava channels is controlled by the slope angle, as pointed out by Harpel et al. (2004). In areas where younger post-caldera flows buried the underlaying caldera rim, lava channels can be traced across the caldera rims (Fig. 14a, Continuous Lava Channels, CLC). Caldera rims are shown as sharp boundaries, where pre-caldera flows, truncated during caldera collapse, are mapped in outcrops (Fig. 14a, Discontinuous Lava Channels, DLC).

The shaded relief DEM also depicts the Camp Flow, a lobate slump feature (rotational slide), originated on the upper flank of the summit cone, as well as linear alignments of vents, trending at N60^{o}E across the summit plateau. Aerial photo interpretation had suggested Camp Flow was a lava flow, hence the name. On close inspection if was discovered the feature was underlain by ice and composed of pyroclastic material, mainly large volcanic bombs. The flow like pattern on the surface resulted from rotational sliding. Later GPS measurements showed the feature was moving down hill at over a cm a year. Fumarole ice towers, typically 2-10 m high and 3-4 m in diameter (David and Priestley, 1909, Holdsworth and Ugolini, 1965; Lyon and Giggenbach, 1974; Giggenbach, 1976), are shown as isolated, small peaks (Fig. 14a, Ice Tower Ridge). Large collapse features, for example on the east flank of the summit cone (Fig. 14a, Large Collapse Feature, LCF), are clearly visible on the shaded relief DEM. It is more difficult to recognize smaller features, such as the snow filled collapse depression SW of the Tramway Ridge (Fig. 14a, Small Collapse Feature, SCF), since these shallow depressions often lack well defined boundaries. Fig. 14b illustrates how this hidden feature can be made visible by using low sun angle and a carefully selected illumination direction.

4.3. Modern-day crater

Prior knowledge about the modern-day summit cone topography was derived from ground observations and from stereo aerial photographs but these only gave imprecise estimates of size and no good data were available on the depth of the lava lake below the crater rim. While the major features of the summit crater have been widely cited, (e.g., Otway et al., 1994), detailed measurements of the crater geometry and depth were lacking.

We employ different visualization techniques and elevation profiles for examining the structure of the summit crater in detail. Fig. 15 presents the ALS DEM as a shaded relief surface (a) and a contour map (b), and shows a color image of the slope map (c). To create the slope map in Fig. 15d, we applied an inverted color scheme and histogram stretching. The resulting image enhances structures on the crater floor. The main lava lake (named Ray Lava Lake) shows up as the small flat area on the NE side of the Inner Crater. The main features of the summit cone are labeled in Fig. 15a. Fig. 16 shows profiles across the Main Crater in NW-SE and SW-NE directions.

The summit of the volcano, 3739.45 m (ellipsoidal height, see also Sec. 3.2.) is situated on the SE part of the crater rim. The Main Crater measures about 570 m by 480 m, and has a flat floor that is divided into two near horizontal benches by a circular fault resulting from collapse. The upper bench is at an elevation of 3595 m and the lower bench is about 10 m below. The Inner Crater occupies the NE part of the Main Crater. The slope maps (Fig. 15c-d) indicate that in December 2001 the Inner Crater had three distinct depressions with horizontal or near-horizontal floor, aligned in NE-SW direction. Ray Lava Lake, a persistent, convecting lava lake, discovered in 1972 (Giggenbach et al. 1973) is located in the NE depression. To provide a quantitative description of all main elements of the Main Crater, we approximated them by analytical functions following the procedure introduced in Sec. 5.2.1-2. For example we delineated lava lakes by fitting horizontal planes and approximated the shape of crater rims by conical segments (Fig. 17). Table 2 summarizes the major parameters (diameter, depth, etc.) of the geomorphologic features of Mount Erebus, including the Main Crater and its structures. Details on the approach and results are given in Sec. 5.

Comparison of an aerial photograph from 4 November 1963 with the ALS DEM indicates significant changes in the morphology and size of the Inner Crater (Fig. 18). In 1963 the Inner Crater had a circular shape while in 2001 it has become larger and more irregularly shaped. The most significant feature is the now oval shaped "Phreatic Crater" SW of the lava lake (Figs. 15-18). The crater formed on 19 October 1993 from two phreatic (steam) eruptions (Dibble et al., 1994), which showered the Main Crater rim with blocks of hydrothermal altered debris. Collapse of the steep walls and the thin septum between the "Phreatic Crater" and the Inner Crater continues to modify them. The Inner Crater has also been enlarged by collapse events of the Inner Crater wall. For example a crater wall collapse event was observed in December 1987, when a 60 m long and 10 m wide, crescent shape segment of the Main Crater floor collapsed into the southern part of the Inner Crater. Further collapse events were observed in February 1989 and in 1995. The Inner Crater floor is also being continually modified by the addition of ejecta (primarily volcanic bombs) from Strombolian eruptions from the lava lake and also by small lava flows erupted from "Werner" vent.

5. Toward automation: Extracting topographic features and surfaces from ALS-DEM

5.1. Rational and principle

Figs. 13-18 show examples of topographic features made "visible" from the DEM by diverse visualization methods. While this representation is very useful for visual inspection, a more quantitative analysis requires the explicit description of features, for example their position, orientation, shape, dimensions, and perhaps their spatial relationships with each other. For a better understanding of the structure and evolution of volcanoes it is therefore of paramount interest to obtain automatically a rich set of topographic features. This section describes our efforts to extract features from surface elevation data, such as the 3D laser point cloud or the high-resolution ALS DEM created from it.

Our topographic feature extraction approach greatly benefits from similar work in computer vision and digital photogrammetry where one goal is to automatically extract man-made objects from such diverse data sets as electro-optical images, 3D laser point clouds, and multi-/hyper-spectral images

(Schenk, 2000; Schenk and Csatho, 2002). To conquer this challenging problem, a multi-stage approach is employed, beginning with extracting geometric primitives (e.g. edge pixels), linking them to features (e.g. edges), followed by approximating them with analytical functions (segmentation) and grouping them to higher level structures that are relevant to a particular application. In this fashion, data is converted to spatial information that enters subsequent reasoning processes. It is important to realize that automatic reasoning (making inferences by computers about objects) cannot be done with raw data, rather it requires explicit information, such as segmented and grouped features, and higher-level constructs.

We apply the same principle to volcanoes by providing specialists quantitative information to aid their analyses. Such information is extracted from surface elevation data and includes geomorphologic features characterizing cones, conic sections, planar and higher order surfaces, lava flows, and other volcanic and structural landforms.

5.2. Fitting analytical functions

5.2.1. Fitting planar surfaces

Our method of extracting relevant volcanic features is based on fitting analytical functions to 3D point clouds or DEMs. A frequently occurring problem is fitting planar or higher order surfaces to 3D points. For example it may be interesting to know if crater or caldera rims are on planar surfaces and how these surfaces are oriented, or to determine the extent and average elevation of a lava lake. In Sec. 3.2 we briefly described the process of fitting a quadratic surface to 3D points for the purpose of interpolating the elevation of a DEM grid post. The unknown coefficients of the surface are obtained by a robust estimation in order to exclude points that may not belong to the surface. In case of a planar surface, Eq. 11 is modified accordingly and only three unknown coefficients must be estimated. The three plane parameters are determined such that the square sum of the orthogonal distances between all points defining the plane and the plane itself becomes a minimum. This fitting method is not only simple but offers the distinct advantage of delivering an error budget. That is, estimated parameters have well defined error bars (variances). The variance component of the adjustment tells how close the data points

are to the fitted plane, referred to as fitting error in this paper.

So far we have assumed that the set of points defining a plane is known. But how do we get these distinct points (usually less than one hundred) from a cloud of 11.7 million points in the first place? Points on a physical plane, for example a lava lake, are characterized by spatial proximity. Thus they can be extracted from the original point cloud by defining a window, preferably smaller than the physical plane because additional points can be added during the fitting process. This region growing method, starting with a seed region, would not work for extracting rim points, however. Rims are characterized by a sudden change of surface slopes. Therefore, rims can be detected from slope images and rim points are then extracted from the laser point cloud or from the DEM. Figs. 8 and 15c-d show examples of rims on slope maps.

5.2.2. Fitting conics and conic sections

The previous sections described the concept of fitting planar or higher order surfaces to 3D data points. We have identified two problems: (i) extracting relevant points from a huge point cloud, (ii) fitting an analytical function to the extracted points in the presence of outliers (points not belonging to the surface). The same principle is applied to fit conics and conic sections.

Circles and ellipses are important features of volcanoes and their automatic detection and parameterization is of interest. A general conic section has eight parameters: three parameters of the plane containing the conic section and five parameters of the (planar) curve. Note that circles and ellipses are degenerated forms of a general conic section and have fewer parameters. We simplify matters by determining the plane and curve parameters separately. After plane fitting, the 3D points are transformed to this plane, reducing the estimation of the curve parameters to a two-dimensional problem. Once again, the target function expresses an explicit relationship of the shortest distance of a (transformed) 2D point to a circle or to an ellipse.

Finally the shape of a volcanic cone can be parameterized by approximating it with a generic cone, described by the 3D position of its tip, the spatial direction of the rotation axis, and the slope angle.

Following a least-squares approach, the six cone parameters are determined such that the square sum of the orthogonal distances of all cone-defining points becomes a minimum. The target function must express the closest distance between a data point and the cone as a function of the six cone parameters.

5.2.3. Results: Characterizing calderas and modern-day crater of Erebus Volcano

We use the procedure outlined above to describe the shape of calderas and craters by conic sections, mainly ellipses and circles. The following list summarizes the procedures for extracting points on the caldera and crater rims starting from the oldest caldera rim.

- Fang Ridge escarpment, which is a manifestation of the proto-Erebus caldera rim (~700 ka): points were extracted from the Ross Island DEM by finding the highest points along the escarpment (Fig. 9a).
- Modern Erebus, older (~90 to 70 ka) and younger (~25 to 11 ka) caldera rims: points on the outcrops of pre-caldera flows, marking the caldera rim, were digitized from the geologic map (Fig. 13, Harpel et al., 2004), and the corresponding elevations were determined from the ALS DEM.
- Main, Inner and "Phreatic" crater rims, Ray Lava Lake and ephemeral lava lake of Werner Vent: points along the rims and within the lava lakes were determined from the ALS DEM by analyzing the changes in surface normal and slope.

Table 2 lists the parameters of the fitted analytical surfaces and curves. It also contains the elevations of the highest and lowest points of each object as well as the deepest point within the structure, if applicable. We used the region growing approach explained in Sec. 5.2.1 for delineating Ray Lava Lake and the ephemeral lake at Werner Vent. First we selected DEM points near the middle of a candidate region based on the enhanced slope map (Fig. 15d, horizontal regions, reddish color), followed by fitting a horizontal plane to these points. Starting from this seed region we added neighboring DEM points as long as their elevations where within ±0.3 m. After accepting a new point, the plane fitting process was

repeated. This region growing process stopped when no new DEM points could be added. The average elevation of the Ray Lava Lake is 3516.0 m and its area is approximately 750 m^2. The Werner vent is smaller, about 166 m^2 and its average elevation of 3515.5 m is quite comparable to that of Ray Lava Lake. The deepest point of the nearby active vent is 3516.5 m, again nearly identical to the average elevation of the Ray Lava Lake. This indicates that at the time of the data acquisition (December 30, 2001) the Ray Lava Lake, Werner Vent and Active Vent were more or less in magmastatic equilibrium. This is an important observation and shows that all the vents are likely to be interconnected at least at depth. It begs the question are the vents in the Inner Crater just small pipes connected at depth (e.g. Fig 20, Aster et al., 2003) or is there a broader widespread shallow magma chamber underlying much of the Inner Crater floor. On the basis of the data here we cannot answer this question but it will be very valuable as we develop models for the conduit system feeding the lava lakes.

Fig. 17 shows the conic segments fitted to the crater rims of modern Erebus cone, while those fitted to the upper part of Fang Ridge (red circle) and to the older and younger modern-Erebus caldera rims (blue circle and pink ellipse) together with their centers are presented on the slope map in Fig. 19. The older modern-Erebus caldera rim is defined by a series of outcrops in the NE part of the Erebus plateau (red outcrops in Figs. 13a and 19). This rim can be closely approximated by a circle – the fitting error for the plane fitting is 18.3 m and for conic (circle) fitting it is 53.6 m. The fitted circle is 50-150 m above the current surface in the S-SW sectors, except for the 1.5 km segment in the SW corner, where the caldera rim is on or near the present day surface. There are not enough well distributed points on the younger modern-Erebus caldera rim to determine a unique solution, but the symmetry of the exposed section indicates that its center was located somewhere near to the N60^{o}E trending, "Ice Tower Ridge" rift zone (Fig. 14a). The pink ellipse, shown in Fig. 19 is a possible, but non-unique solution.

5.3. Combination of geomorphometric mapping and surface fitting for extracting lava channels

The automatic detection and characterization of lava channels is a more complex endeavor than the extraction of simple features discussed so far. However, the first step is identical: extract from the

point cloud or DEM those points that belong to a lava channel. The geomorphometric map introduced in Sec. 3.5. is a good starting point for delineating lava channels automatically. Lava channels are characterized by parallel arrangements of ridge points separated by channel points. Fig. 11d shows several well-developed NW trending lava channels on the NW flank of the volcano as parallel blue ridge-lines separated by orange channel regions corresponding to the interior of the lava channels. Extraction is also guided by domain knowledge (e.g., lava flows more or less in direction of the steepest gradient). Before extracting points within a delineated area of a lava channel it may be advisable to inspect and possibly edit the area. Once points in a designated area are extracted, an approximate flow direction is determined, followed by defining cross-sections at given intervals along the flow direction. The cross-sections, perpendicular to the flow direction, have a specified width and are centered at the channel. Although the distance between successive cross-sections and their width are specified a priori, it is possible to change the values during processing time if current knowledge justifies it.

At this stage, cross-sections are defined by their end points: left-most and right-most point as viewed in the direction of the channel. With these two points, elevations at regular distances are determined from the DEM. The resulting sequence of points is now approximated by a third order polynomial, following the fitting procedure discussed earlier. The inflection points of the fitted polynomial, which are characteristic features of a lava channel, can easily be determined from the estimated coefficients or as zero crossings of the derivatives. Moreover, geomorphological features, such as channel width and depth, can be derived from the fitted polynomials.

We demonstrate the extraction of lava channels on the prominent ridge of the Tramway Ridge Flow, NW of the summit. Fig. 20a shows the geomorphometric classification map of the NW summit plateau draped on the surface topography with blue pixels marking ridges and the bright yellow pixels indicating channels. The red box marks the area where elevation profiles, perpendicular to the lava flow directions are extracted. The length of these elevation profiles, shown in Fig. 20b, is selected so that they cover the levees and part of the outer slope of the flow. After the polynomials are fitted, the width of the channel is determined as the distance between the maximums and the depth of the channel is determined

by computing the average difference between the peak elevations and the lowest point of the channel.

6. Conclusions

This study has provided the first high precision topographic data on the dimensions and topography of the Main Crater and especially the Inner Crater of Erebus volcano. The Inner Crater is dynamic and difficult to observe from the ground and this study demonstrates the value of lidar as a mapping tool. The lidar-derived DEM will be valuable as a baseline and its value will grow if and when further lidar surveys are made and can be used with this work to quantify changes in the lava lakes and crater morphology. The ability to do quantitative geomorphological observations on an active volcano are clearly demonstrated. Especially valueable are the measured surface areas of the lave lakes as this controls thermal emissions and gas fluxes from the volcano.

Volcanic calderas and craters appear to be oval but their rims often have a more complex shape. Rims are usually not confined to a planar surface as they are breached contemporaneously or after crater formation. Despite this complexity, conic sections, such as circles and ellipses approximate crater rims quite well. A good example is the small fitting error of a circle fitted to the older modern-Erebus caldera rim (Sec. 5.2.3.). The parameters of fitted conic sections and their defining planes provide concise descriptions of caldera and crater rims in 3D. Major and minor axes and their ratios characterize size and elongation of rims and the surface normal of the plane containing the conic section describes the 3D orientation of the rim (Table 2).

Closer inspection of conic sections fitted to visible segments of a caldera may help identifying other, less prominent portions of the caldera. Such portions may be partially buried under younger lava flows or may be covered by ice and snow (typical on Mount Erebus). An interesting example of a previously undetected section of the proto-Erebus caldera rim is on the NE flank of Erebus. Here, the reconstructed crater rim from the Fang Ridge (Fig. 19) coincides with pronounced changes in slope at elevations between 2900 and 3100 m, suggesting the location of a caldera rim segment. We also analyzed the geometry of the older modern-Erebus caldera rim in a similar fashion. Harpel et al. (2004) suggested

that the summit region of Erebus is composed from two superimposed calderas and interpreted a prominent break in slope on the southwestern side of the summit plateau as the expression of these juxtaposed caldera rims. The change in slope below the younger modern-Erebus caldera rim where the plane of the older caldera rim intersects the SW flank of the volcano at an elevation of 3 200 m confirms this interpretation (Fig. 21).

The center of the conic section fitted to a caldera rim, the caldera center, may approximate the location of the main vent at the time of the caldera collapse event (Esser et al., 2004). During the proto-Erebus caldera collapse event the inferred caldera center was located 1.75 km north of the current summit vent (Fig. 19). During the older modern-Erebus caldera collapse event, 90-70 ka ago, the caldera center and thus the presumed vent was closer, about 1 km north of the modern summit caldera and at the time of the younger modern-Erebus caldera collapse event 11-25 ka ago the caldera center was only slightly offset to the north from the current position.

The linear alignments on the summit plateau (Fig. 8) and the walls of the Main Crater of the Erebus volcano (Figs. 17-18) show good agreement with previously mapped faults and dykes within the Erebus volcanic province (Kyle, 1990b; Wilson and Demosthenous, 2000). For example, the rift zone of Ice Tower Ridge, trending at N60^{o}E across the summit plateau (Figs. 8 and 14a) follows the trend of an inferred major transfer or transform fault connecting the peaks of Mt Morning and Discovery and possibly terminating the Terror rift (Kyle, 1990b). Similarly trending volcanic cone alignments were mapped on the east flank of Mount Terror by Wilson and Demosthenous (2000). Several other lineaments, trending N24^{o}E, E16^{o}S and E44^{o}S, can be traced on the summit plateau (Fig. 8).

Airborne lidar surveys provide high resolution, accurate topographic data over large areas. While digital elevation data are very effective for mapping geomorphic features and for visualizing landforms, the real potential lies in the extraction of topographic features and in their perceptual organization to structures that are meaningful and rich in spatial information for the subsequent analysis by specialists. Work reported in this paper clearly demonstrates the advantage of an interdisciplinary approach to conquer the challenges of automating feature extraction and grouping processes. Motivated by the success

of incorporating information from different sensors and sources we will continue our research in sensor and information fusion and focus on the automatic detection and delineation of lava channels.

Acknowledgement

We thank members of NASA's ATM group for collecting and processing the ATM data. Taehun Yoon (UB) and students of OSU photogrammetry group assisted in generating the DEM. We thank Raytheon Polar Services and especially PHI for field and helicopter support, and Mike Willis (OSU), Beth Bartel (UNAVCO) and Mark Murray (NMT) for processing ground GPS observations. C. Hallam (USGS) provided quality checking and dissemination of the DEMs via the Antarctic Atlas of USGS. Reviews by Richard Aster and Clive Oppenheimer help improve the final version of the manuscript. BC, TS and WK were supported by NSF grant OPP-0233246 and by NASA's ICESat program. PK was supported by NSF grants OPP-0229305 and ANT-0538414. GPS data were made available by UNAVCO, Landsat and ASTER satellite imagery and aerial photographs are from USGS.

References:

Adiyaman, Ö., Chorowicz, J., Köse, O., 1998. Relationship between volcanic patterns and neotectonics in Eastern Anatolia from analysis of satellite images and DEM. Journal of Volcanology and Geothermal Research 85:17-32.

Aster, R., Mah, S., Kyle, P., McIntosh, W., Dunbar, N., Johnson, J., Ruiz, M., McNamara, S., 2003. Very long period oscillations of Mount Erebus Volcano, J. Geophys. Res., 108(B11), 2522, doi:10.1029/2002JB002101.

Aster, R., McIntosh, W., Kyle, P., Esser, R., Bartel, B., Dunbar, N., Johns, B., Johnson, J., Karstens, R., Kurnik, C., McGowan, M., McNamara, S., Meertens, C., Pauly, B., Richmond, M., Ruiz, M., 2004. Real time data received from Mount Erebus Volcano. Antarctica, Eos, Trans. AGU 85(10): 97-104.

Bartel, B., Kyle, P.R., Desmarais, E., Meertens, C., Kurnik, C., Johns, B., 2003. Campaign and continuous GPS measurements of deformation at Mt. Erebus, Antarctica. IX International Antarctic Earth Science Symposium, Potsdam.

Behrendt, J., 1999. Crustal and lithospheric structure of the West Antarctic Rift System from geophysical investigations - a review. Global and Planetary Change 23: 25-44.

Carter, W., Shrestha, R., Tuell, G., Bloomquist, D., Sartori, M. 2001. Airborne laser swath mapping shines new light on Earth's topography. Eos, Trans. AGU 82(46): 549-550, 555.

Cotton, C.A. 1944. Volcanoes as Landscape Forms. Whitcombe and Tombs Publ., Christchurch, 416 p.

Csatho, B., Lee, Y-R., Schenk, T., Krabill, W., McGarry, J., 2001. Creation of high resolution Digital Elevation Models (DEM) of Ocean City and Assateague Island, MD. International Archives of Photogrammetry and Remote Sensing 34(3 W4): 31-35.

Csatho, B., Schenk, T., Krabill, W., Wilson, T., Lyons, W., McKenzie, G., Hallam, C., Manizade, S., Paulsen, T., 2005. Airborne Laser Scanning for high-resolution mapping of Antarctica. Eos, Trans. AGU 86(25): 237-238.

Cunningham, D., Grebby, S., Tansey, K., Gosar, A., Kastelic, V., 2006. Application of airborne LiDAR to mapping seismogenic faults in forested mountainous terrain, southeastern Alps, Slovenia. Geophysical Research Letters 33, L20308, doi:10.1029/2006GL027014.

Davies, A.G., Calkins, J., Scharenbroich, L., Vaughan, R.G., Wright, R., Kyle, P**.,** Castańo, R., Chien, S., Tran, D., 2008. Multi-Instrument Remote and In Situ Observations of the Erebus Volcano (Antarctica) Lava Lake in 2005: a Comparison with the Pele Lava Lake on the Jovian Moon Io. Journal of Volcanology and Geothermal Research (this volume).

David, T.W.E., Priestley, R.E., 1909. Notes in regard to Mount Erebus. In Shackleton, E.H. The Heart of the Antarctic vol. 2, William Heinemann, London, pp. 308-310.

Dibble, R.R., Kyle, P.R., Skov, M., 1994. Volcanic activity and seismicity of Mount Erebus. 1986-1994, Antarctic Journal of the U.S. 29: 11-14.

Dora, M., 2005. A geomorphologic extraction method for mapping glacier-induced features from high resolution topographic data in the Dry Valleys area, Antarctica. MS Thesis, Technische Universität Dresden, 120 pages.

Esser, R.E., Kyle, P.R., McIntosh, W.C., 2004. $^{40}Ar/^{39}Ar$ dating of the eruptive history of Mount Erebus, Antarctica: volcano evolution. Bulletin of Volcanology 66: 671-686.

Favalli, M., Innocenti, F., Pareschi, M.T., Pasquare, G., Mazzarini, F., Branca, S., Cavarra, L., Tibaldi, A., 1999. The DEM of Mt. Etna: geomorphological and structural implications. Geodinamica Acta (Paris) 12(5): 279-290.

Finnegan, D.C., Ghent, R.R., Bymes, J.M., Burke, M. 2004. Morphometric LiDAR analysis of Amboy Crater, California: Application to MOLA analysis of analogue features on Mars. Lunar and Planetary Science XXXV, abstract no. 1736, Lunar and Planetary Institute, Houston.

Giggenbach, W.F., 1976. Geothermal ice caves on Mt Erebus, Ross Island, Antarctica. New Zealand Journal of Geology and Geophysics 19 (3): 365-72.

Giggenbach, W.F., Kyle, P.R., Lyon, G., 1973. Present volcanic activity on Mt. Erebus, Ross Island, Antarctica. Geology 1: 135-136.

Harpel, C.J., Kyle, P.R., Esser, R.P., McIntosh, W.C., Caldwell, D.A., 2004. $^{40}Ar/^{39}Ar$ dating of the eruptive history of Mount Erebus, Antarctica: summit flows, tephra, and caldera collapse.

Bulletin of Volcanology 66: 687-702.

Haugerud, R., Harding, D. J., Johnson, S. Y., Harless, J. L., Weaver, C. S., and Sherrod, B. L., 2003. High-resolution lidar topography of the Puget Lowland, Washington. A bonanza for Earth science. GSA Today 13(6): 4-10.

Hofton, M.A., Malavassi, E., Blair, J.B., 2006. Quantifying recent pyroclastic and lava flows at Arena Volcano, Costa Rica, using medium footprint lidar. Geophysical Research Letters 33, L21306, doi:10.1029/2006GL027822.

Holdsworth, G., Ugolini, F.C. 1965. Fumarolic ice towers on Mt. Erebus, Ross Island. Antarctica. Journal of Glaciology 1: 135-6.

Hubbard, B.E., Sheridan, M.F., Carrasco-Núñez, G., Diaz-Castellón, R., Rodriguez, S.R., 2007. Comparative lahard hazard mapping at Volcan Citlaltépetl, Mexico, using SRTM, ASTER and DTED-1 digital topographic data. Journal of Volcanology and Geothermal Research 160: 99-124.

Kelly, P., Dunbar, N., Kyle, P., McIntosh, W., 2008. Refinement of the younger geologic history of Erebus volcano, Antarctica using $^{40}Ar/^{39}Ar$ and ^{36}Cl age determinations. Journal of Volcanology and Geothermal Research (this issue).

Kervyn, M., Kervyn, F., Goossens, R., Rowland, S.K., Ernst, G.G.J., 2007.Mapping volcanic terrain using high-resolution and 3D satellite remote sensing. In R.M. Teeuw (Editor), Mapping Hazardous Terrain using Remote Sensing, Geological Society, London, Special Publications 283: 5-30.

Köster, K., Spann, M., 2000. Mir: an approach to robust clustering – application to range image segmentation. IEEE Transactions on Pattern Analysis and Machine Intelligence 22(5): 430-444.

Krabill, W.B., Abdalati, W., Frederick, E.B., Manizade, S.S., Martin, C.F., Sonntag, J.G., Swift, R.N., Thomas, R.H., Yungel, J.G., 2002. Aircraft laser altimetry measurement of elevation changes of the Greenland ice sheet: technique and accuracy assessment. Journal of Geodynamics 34: 357-376.

Kyle, P.R., Dibble, R.R., Giggenbach, W.F., Keys, J., 1982. Volcanic activity associated with the anorthoclase phonolite lava lake, Mt. Erebus, Antarctica. In C. Craddock (Editor), Antarctic Geosciences, University of Wisconsin Press: 735-745.

Kyle, P. R., 1990a. McMurdo Volcanic Group, western Ross Embayment: Introduction. In W. E. LeMasurier and J. W. Thomson (Editors), Volcanoes of the Antarctic Plate and Southern Oceans, Antarctic Research Series, AGU, Washington, D. C., 48: 19-25.

Kyle, P.R., 1990b. Erebus Volcanic Province. In W. E. LeMasurier and J. W. Thomson (Editors), Volcanoes of the Antarctic Plate and Southern Oceans, Antarctic Research Series, AGU, Washington, D. C., 48: 81-88.

Kyle, P.R., Moore, J.A., Thirlwall, M.F., 1992. Petrologic evolution of anorthoclase phonolite lavas at Mount Erebus, Ross Island, Antarctica. Journal of Petrology 33: 849–875.

Kyle, P.R., Merteens, C., Johns, B., Desmarais, E., Kurnik, C., Aster, R., 2001. The Mount Erebus GPS Array. In Search of Volcanic Deformation, Antarctic Neotectonics Workshop, Abstracts & Program, Terra Antarctica Publication, Siena, Italy.

Lee, Jong-Sen, 1980. Digital Image Enhancement and Noise Filtering by Use of Local Statistics. IEEE Transactions on Pattern Analysis and Machine Intelligence 2: 165-168.

Lemoine, F.G., Pavlis, N.K., Kenyon, S.C., Rapp, R.H., Pavlis, E.C., Chao, B.F., 1998. New high-resolution model developed for Earth' gravitational field. EOS, Trans. AGU 79(113): 117-118.

Lyon, G.L., Giggenbach, W.F. 1974. Geothermal activity in Victoria Land, Antarctica. New Zealand Journal of Geology and Geophysics 17(3): 511-21.

Mazzarini, F., Pareschi, M.T., Favalli, M., Isola, I., Tarquini, S., Boschi, E., 2005. Morphology of basaltic lava channels during the Mt. Etna September 2004 eruption from airborne laser altimetry data. Geophysical Research Letters 32, L04305, doi:10.1029/2004GL021815.

Mazzarini, F., Pareschi, M.T., Favalli, M., Isola, I., Tarquini, S., Boschi, E., 2007. Lava flow identification and aging by means of lidar intensity: Mount Etna case. Journal of Geophysical Research 112, B02201, doi:10.1029/2005JB004166.

Moore, J.A., Kyle, P.R., 1987. Volcanic geology of Mt. Erebus, Ross Island, Antarctica. Proceedings of NIPR Symposium on Antarctic Geoscience 1:46-65.

Moore, J.A., Kyle, P.R., 1990. A.17. Mount Erebus. In W. LeMasurier, J. Thompson (Editors), Volcanism of the Antarctic Plate and Southern Oceans, Antarctic Research Series, 48, AGU: 103-108.

Otway, P.M., Blick, G.H., Scott, B.J. 1994. Volcanic deformation monitoring on Mount Erebus: methods and results of geodetic surveys, 1980-85. In P. Kyle (Editor), Volcanological and environmental studies of Mount Erebus, Antarctica, Antarctic Research Series, 66, AGU: 57-68.

Rothery, D.A., Oppenheimer, C., 1994. Monitoring Mount Erebus by satellite remote sensing. In P. Kyle (Editor), Volcanological and environmental studies of Mount Erebus, Antarctica, Antarctic Research Series, 66, AGU: 51-56.

Schenk, T., 2000. Object recognition in digital photogrammetry. Photogrammetric Record 16(95): 743-762.

Schenk, T., Csatho, B., 2002. Fusion of lidar data and aerial imagery for a more complete surface description. International Archives of Photogrammetry and Remote Sensing 34(3A): 310-317.

Schenk, T., Csatho, B., Ahn, Y., Yoon, T., 2004. Antarctic DEM site reports. Published online by USGS, http://usarc.usgs.gov/lidar/Site_reports/, 48 pages.

Thouret, J.-C. 1999. Volcanic geomorphology—an overview. Earth-Science Reviews 47, 95–131.

Ventura, G., Vilardo, G., 2008. Emplacement mechanism of gravity flows inferred from high resolution Lidar data: The 1944 Somma–Vesuvius lava flow (Italy) Geomorphology 95, 223–235.

Webster, T.L., Murphy, J.B., Gosse, J.C., 2006. Mapping subtle structures with light detection and ranging (LIDAR): flow units and phreatomagmetic rootless cones in the North Mountain Basalt, Nova Scotia. Canadian Journal of Earth Sciences 43: 157-176.

Wehr, A., Lohr, U., 1999, Airborne laser scanning—An introduction and overview. J. Photogramm. Remote Sens., 54, 68– 82.

Willis, M.J., Wilson, T.J., James, T.S., 2006. Bedrock motion from a decade of GPS measurement in Southern Victoria Land, Antarctica. EOS, Trans. AGU 87(52), Fall Meet. Suppl., Abstract G33B-0059.

Wilson, T.J., Demosthenous, C.M., 2000. SAR-based mapping of glaciated volcanic terrain: the Erebus volcanic province, Antarctica. Canadian Journal of Remote Sensing 26(2):142-158.

Wood, J., 1996. The Geomorphological Characterization of Digital Elevation Models. Ph.D. Dissertation, University of Leicester, Department of Geography, Leicester, UK.

Wright, R., Pilger, E., 2008. Satellite observations reveal little inter-annual variability in the radient flux from the Mount Erebus lava lake, Journal of Volcanology and Geothermal Research (this volume).

Figure captions

Fig. 1. Shaded relief representation of Ross Island DEM created by merging the 1:50,000 scale digital contour map of USGS-LINZ with the ALS DEM. Contour lines are at 0, 500, 1000, 1500 and 2000 m elevations. Boxed area is ALS DEM, shown in Fig. 7.

Fig. 2. Principle of airborne laser scanning. The position of a laser point (**p**) is obtained from the GPS vector (**g**) and the range vector (**r**).

Fig. 3. Plotted are the positions of laser points of two consecutive scans obtained during an Erebus mission.

Fig. 4. (a) Illustration of the impact of a directional error, σ_d, on the laser point accuracy. It causes a lateral displacement of the laser beam, Δs, which is decomposed into a horizontal and vertical error component Δp_d and Δz_d. In (b) the impact of a range error, σ_r, on the laser point accuracy is shown. It changes the range r and causes a horizontal and vertical point error Δp_r and Δz_r as a function of the scan angle α. (c) illustrates the impact of a horizontal laser point error on the elevation, called secondary elevation error here.

Fig. 5. Flight trajectories over Mount Erebus (blue lines), NASA's ATM data acquisition, December 30, 2001, shown on ASTER satellite imagery acquired on January 9, 2006 (band 3N).,

Fig. 6. Illustration of orthometric and ellipsoidal heights.

Fig. 7. ALS DEM of the Erebus summit plateau in color with 50 m elevation contours. Labels mark the GPS sites used for accuracy assessment in Table 1. Background is a shaded relief representation of the Ross Island DEM. Highlighted area is shown in Fig. 11. Black and white lines indicate profiles presented in Fig. 12. and 21, respectively.

Fig. 8. Slope map computed from ALS DEM. Large arrow points to Ice Tower Ridge rift zone and small arrows indicate other linear alignments. White curves mark caldera rims mapped by Harpel et al., 2004.

Fig. 9. (a) 3D visualization of Mount Erebus, created from Ross Island DEM; (b) Slope map of Mount Erebus, contour lines are are at 500, 1000, 1500, 2000, 2500 and 3000 m elevations. White line marks the

elevation of 1500 m, the highest elevation where the proto-Erebus shield phase is exposed. Black lines mark profiles shown in Fig. 12 and 21.

Fig. 10. Illustration of the DEM error *d*, shown as the difference of a DEM grid point on the fitted surface to the topographic surface. The DEM error depends on the error of the fitted surface which, in turn, depends on the laser point accuracy, *e*, and the distribution of the laser points. The fitting error, *f*, is related to the laser point accuracy and to closeness of the mathematical model of the fitted surface to the shape of the true surface.

Fig. 11. Maps derived from the ALS DEM and other data sets from the ATM laser scanning system on the NW flank of Mt. Erebus (location is shown in Fig. 7). (a) Color elevation map; (b) shaded relief representation of color elevation map; (c) slope map derived from ALS DEM by applying a 3x3 (6 m x 6 m) template; (d) morphometric features computed from the ALS DEM: ridge pixels are blue, channels are ocher, planes are light green. Kernel size is 12 m and regions smaller than 30 pixels are labeled as unclassified (white); (e) reflected solar radiation image from the ATM passive channel (uncalibrated); (f) details of an aerial photograph acquired on February 20, 1982 (TAM2503_f32V_67 from United States Antarctic Resource Center).

Fig. 12. Topographic expression of the evolution of Erebus volcano illustrated by a NNE-SSW elevation profile extracted from the Ross Island DEM (location is shown in Fig. 7 and 9b).

Fig. 13. (a) Geologic map of the summit plateau from Harpel et al. (2004); (b) 3D representation of the ALS DEM showing the oucrops of pre-caldera flows around the caldera rim; (c) geologic map draped on a 3D representation of the ALS DEM.

Fig. 14. (a) Shaded relief DEM of the summit plateau, illumination is from NE, sun angle is 45º. Marked features: Continuous Lava Channels, CLC, Discontinuous Lava Channels, DLC; Large Collapse Feature, LCF; Small Collapse Feature, SCF; (b) Shaded relief DEM of Tramway Ridge with a sun angle of S270^{o}W. Note the improved detection of the snow filled collapse feature SW of the Tramway Ridge Flow.

Fig. 15. Topography of the modern crater of Erebus. (a) Shaded relief representation of ALS DEM with

major geomorphological features labeled; (b) contour map representation of ALS DEM with white lines marking the profiles shown in Fig. 16; (c) slope map; (d) slope map created by using an inverted color scheme and histogram stretching to enhance structures on the crater floor.

Fig. 16. Elevation transects across the Main Crater of Mount Erebus (locations are shown in Fig. 15b).

Fig. 17. Shaded relief color contour map representation of ALS DEM around the crater showing fitted conical sections approximating the rims of the Main (yellow), Ray Lava Lake (red) and "Phreatic" craters (blue).

Fig. 18. Main Crater of Erebus (a) shown in a 1963 aerial photograph (TMA1214_F32_4, from United States Antarctic Resource Center); (b) 3D representation of ALS DEM, December 30, 2001.

Fig. 19. (a) Summary plot of volcanic features extracted from the Ross Island and ALS DEMs. Solid color curves are conic segments fitted to caldera and crater rims: Fang Ridge (red), older modern-Erebus caldera rim (blue) and younger modern-Erebus caldera rim (pink). Dark gray, light gray and white parts of blue conic indicates where the fitted ellipse is 0-50 m, 50-100 m and > 100 m above the current surface. Symbols mark inferred vent locations and black dotted line is the Ice Tower Ridge rift zone described by Otway et al. (1994).

Fig. 20. Extraction of lava channels parameters from the ALS DEM. (a) Geomorphometric features extracted from the ALS DEM draped on the shaded relief DEM. Blue color marks ridge points, bright yellow regions are channels. Red box marks section of Tramway Ridge Flow, examined in detail in (b), highlighted is the area shown in Fig. 11; (b) elevation profiles across Tramway Ridge Flow with fitted polynomials. The red curve is the first derivative of the polynomial and its zero-crossings, marked by blue dots, indicate extrema, such as the top of lava levees and the bottom of lava channels.

Fig. 21. WSW-ENE elevation profile across the Main Crater showing the surface expressions of the older and younger modern-Erebus caldera rims and the plane of the older caldera rim determined by surface fitting (location is shown in Fig. 7, white line and in Fig. 9b).

Tables:

Table 1

DEM quality control with 13 GPS observations. GPS positions and elevations are given in WGS-84 reference system. h_{DEM} is computed by bilinear interpolation from the ALS DEM at the locations of the GPS stations.

Station ID	Latitude (°)	Longitude (°)	H_{GPS} (m)	**Error! Objects cannot be created from editing field codes.** (m)	Type	Terrain	Processed by
CONZ	167.085476	-77.534592	3402.85	-0.06	continuous	Flat	M. Willis, OSU
E1G2	167.139553	-77.530377	3654.32	0.00	continuous	Flat	M. Willis, OSU
EAST	167.224704	-77.519378	3391.86	1.49*	campaign	Cliff	M. Murray, NMT
E1GP	167.138980	-77.530001	3648.85	0.58	continuous	Flat	B. Bartel, UNAVCO
ELHT	167.146100	-77.510448	3347.31	0.32	campaign	Flat	M. Willis, OSU
ERE0	167.153468	-77.511132	3356.75	0.12	campaign	Flat	M. Willis, OSU
ERE1	167.147947	-77.511400	3361.29	0.82	campaign	Ridge	M. Willis, OSU
ERE2	167.156133	-77.511168	3355.54	0.50	campaign	Ridge	M. Willis, OSU
ERE3	167.151400	-77.509756	3348.48	0.86	campaign	Ridge	M. Willis, OSU
HELZ	167.177548	-77.505253	3301.34	0.27	campaign	Flat	M. Murray, NMT
LEHG	167.141075	-77.510663	3346.15	0.54	continuous	Flat	M. Willis, OSU
NAUS	167.147143	-77.521960	3 572.08	0.67	continuous	Flat	M. Willis, OSU
RAYG	167.170576	-77.528772	3 715.15	0.01	continuous	Flat	M. Willis, OSU

$\Delta h = h_{GPS} - h_{DEM} = 0.32 \pm 0.39$ m

- Station EAST, located near the edge of a cliff is not included in the statistics.

Table 2.

Parameters, describing the shape of the volcanic features of Erebus volcano, derived by fitting analytical curves and surfaces.

Feature	Shape	Fitted plane		Fitted conic within plane			Lowest point	Highest point	Deepest point within structure
		Dip (º)	Dip direction relative to N (º)	Major axis (m)	Minor axis (m)	Elongation relative to N (º)	Elevation (m, WGS-84)		
Fang Ridge	Circle			6700		N/A	?	3082	N/A
Modern-Erebus, older caldera rim	Circle	3.4	290	4294		N/A	3133	3433	N/A
Modern-Erebus, younger caldera rim	Ellipse	Not enough data to determine					3386	3424	N/A
Main Crater rim	Ellipse	7	306	566	481	30	3685	3740	3513
Inner Crater rim	Ellipse	4.6	210	263	247	120	3580	3600	3513
Ray Lava Lake, crater rim	Ellipse	0	N/A	67	54	120	3530	3530	3517
Ray Lava Lake, surface	Irregular	0		N/A			3514.5	3517	3514.5
Werner Vent, ephemeral lake	Irregular	0		N/A			3514.5	3516	3514.5
Active Vent	Point	N/A		N/A			3516.5		3516.5
“Phreatic Crater” rim	Ellipse	6	315	93	70	135	3580	3592	3523

Fig.1

Fig. 1.

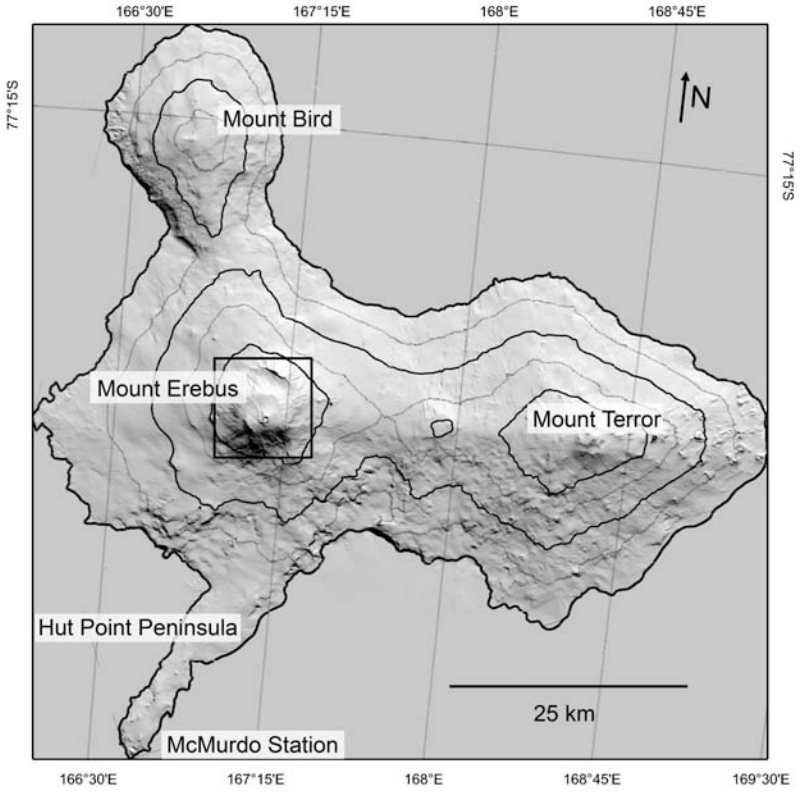
166°30'E
167°15'E
168°E
168°45'E
77°15'S
N
Mount Bird
Mount Erebus
Mount Terror
Hut Point Peninsula
25 km
McMurdo Station
169°30'E

Fig. 2

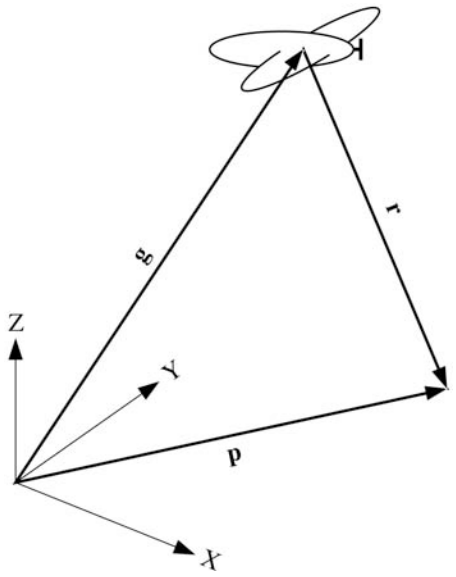

Fig. 3

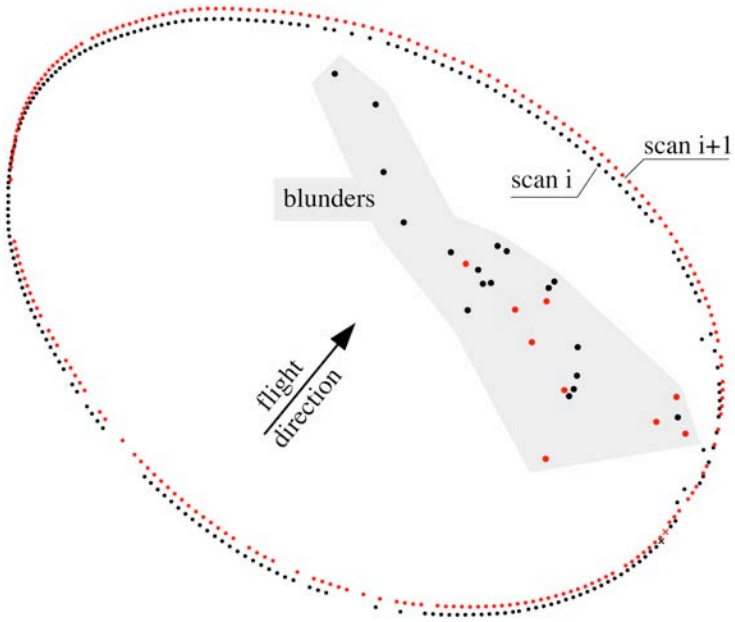

Fig. 4

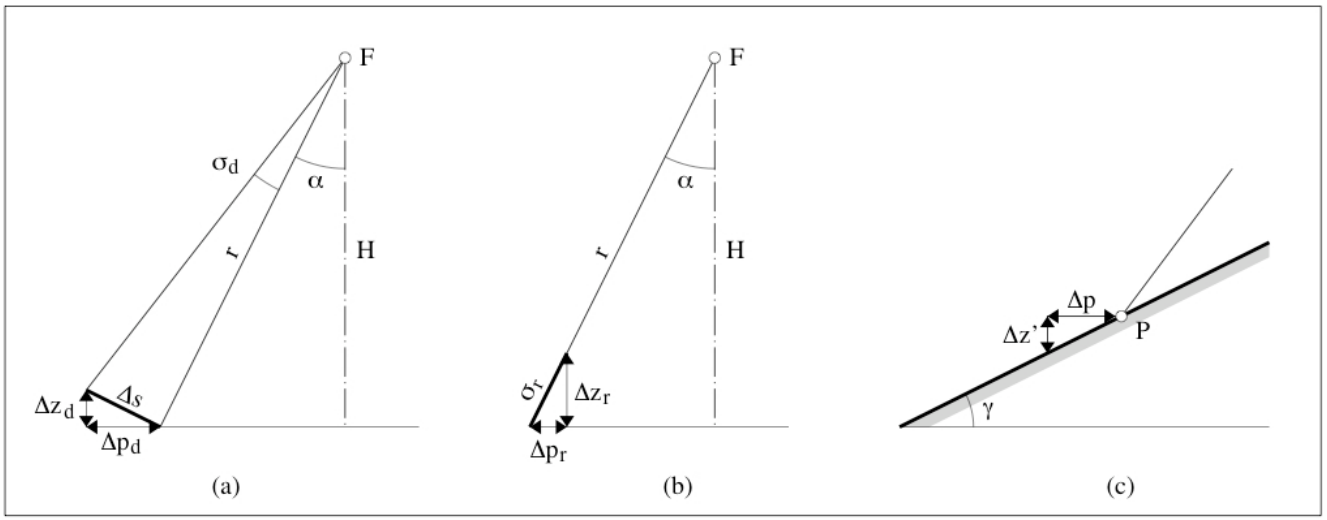

Fig. 5

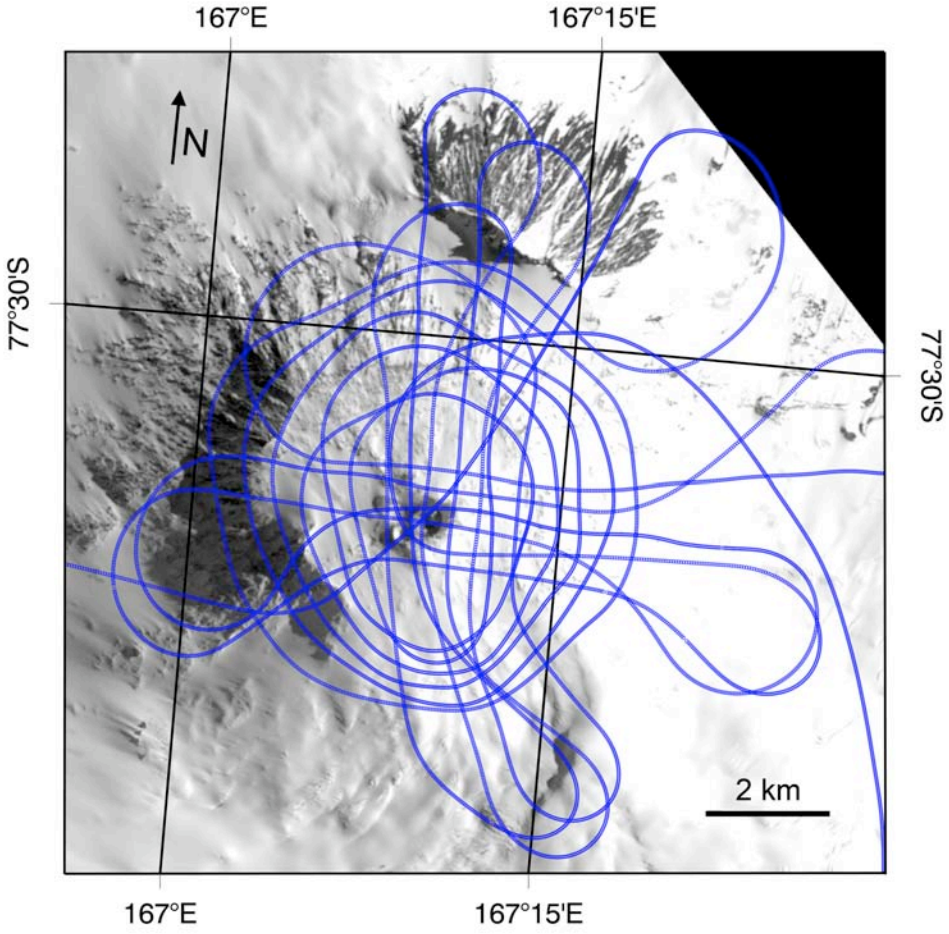

Fig. 6

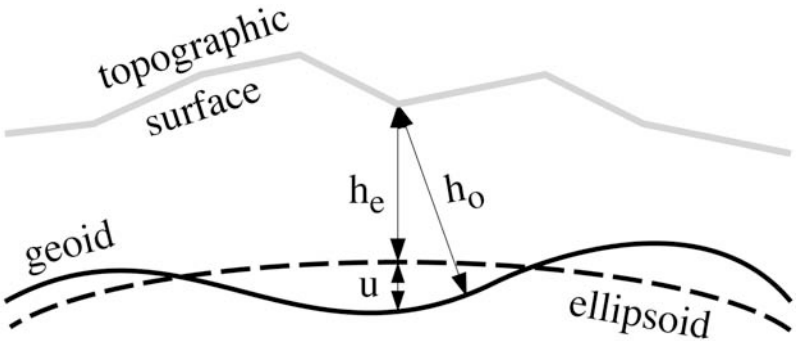

Fig. 7

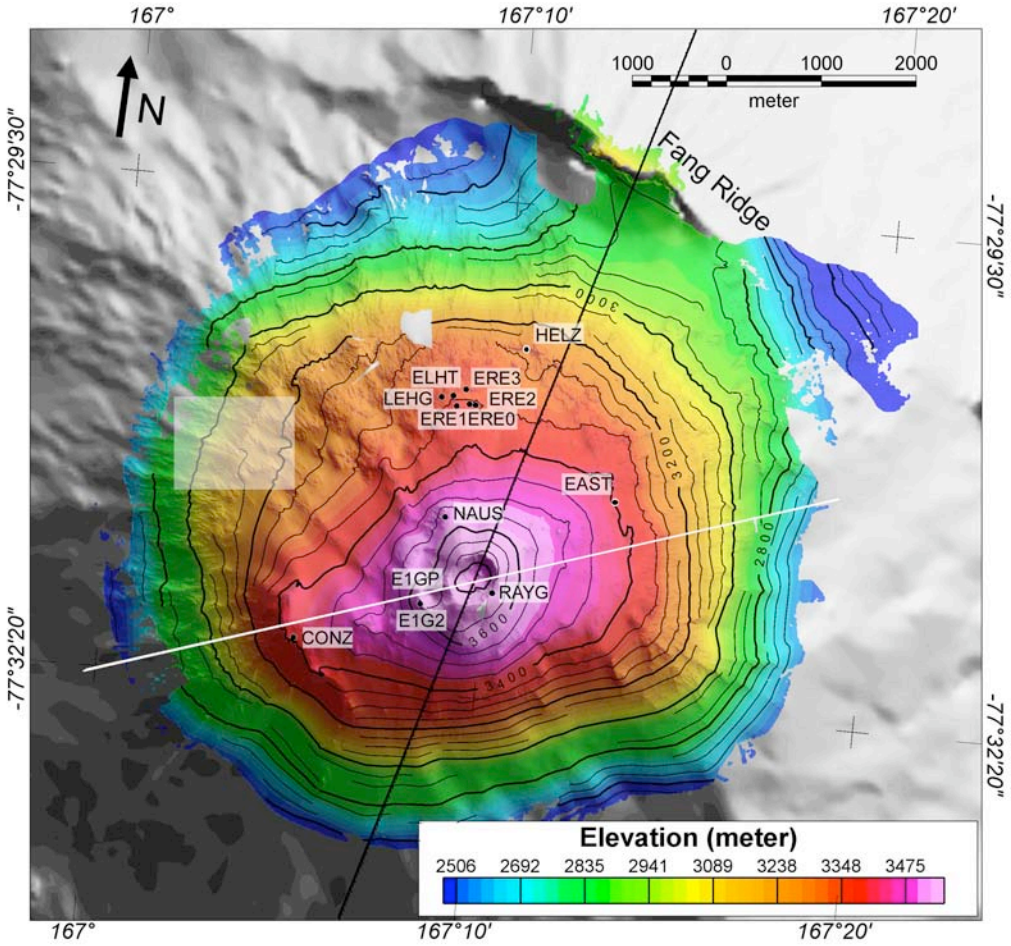
167°
167°10′
167°20′
-77°29′30″
-77°32′20″
N
1000 0 1000 2000
meter
Fang Ridge
HELZ
ELHT
ERE3
LEHG
ERE2
ERE1
ERE0
EAST
NAUS
E1GP
RAYG
E1G2
CONZ
3000
3200
3400
3600
2800
Elevation (meter)
2506 2692 2835 2941 3089 3238 3348 3475

Fig. 8

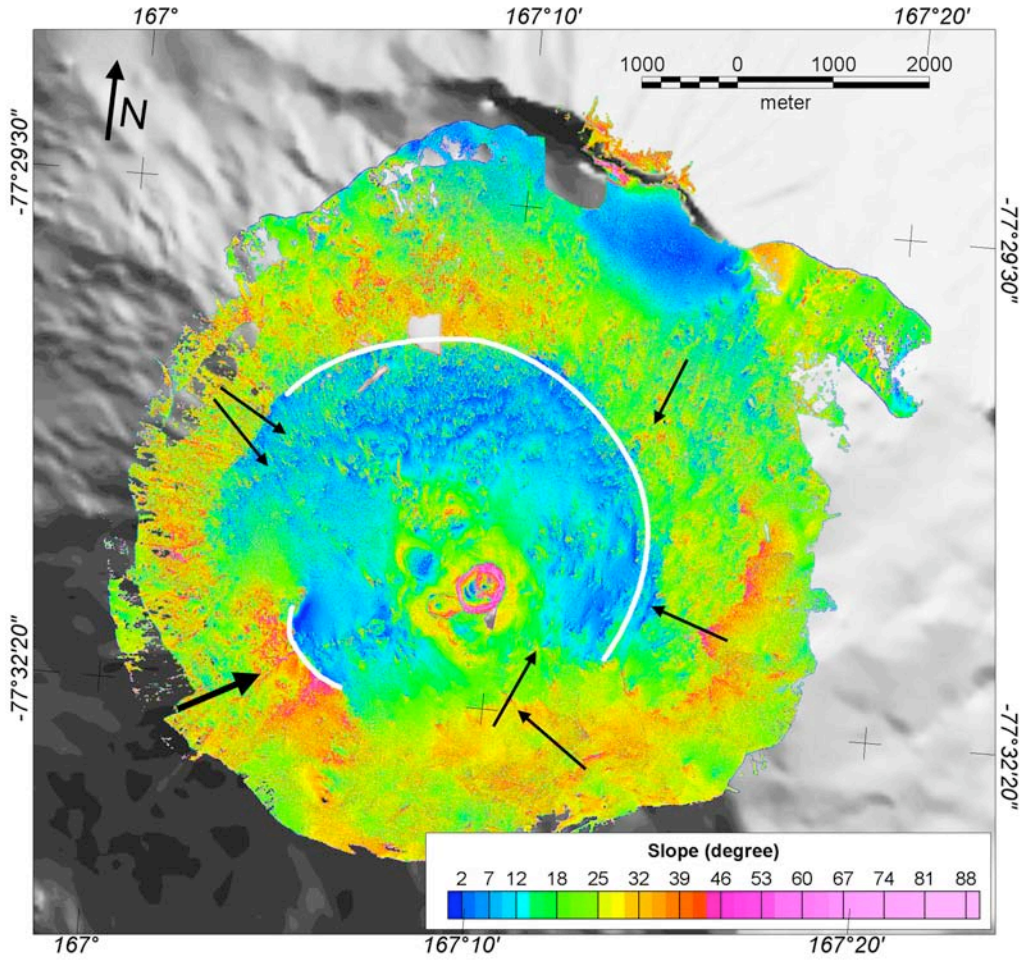
167°
167°10′
167°20′
1000 0 1000 2000
meter
N
-77°29′30″
-77°32′20″
Slope (degree)
2 7 12 18 25 32 39 46 53 60 67 74 81 88

Fig. 9

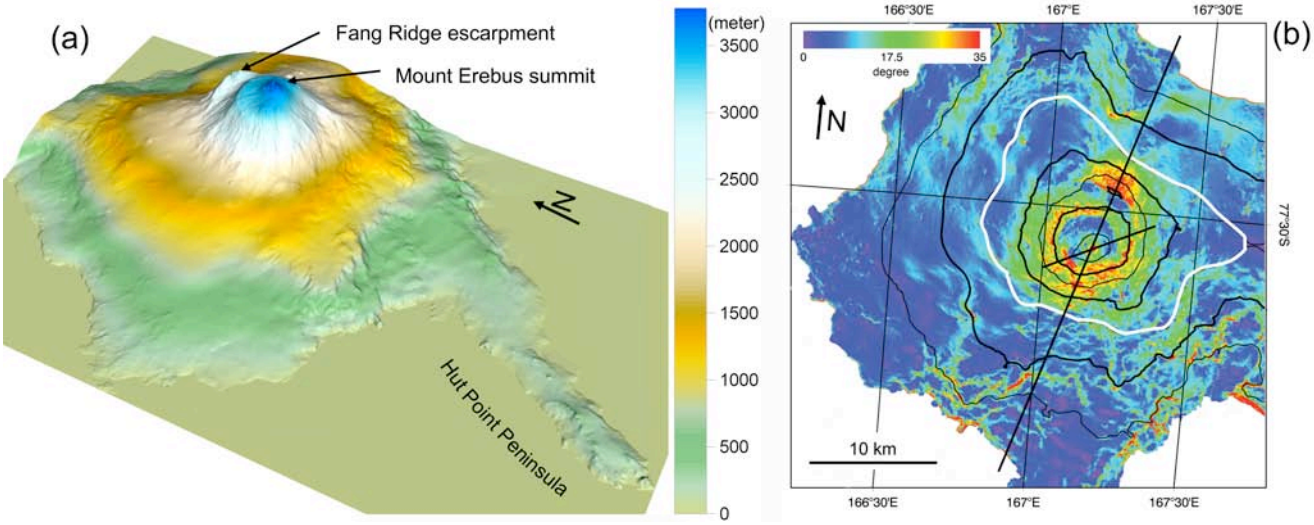
(a)
Fang Ridge escarpment
Mount Erebus summit
N
Hut Point Peninsula
(meter)
3500
3000
2500
2000
1500
1000
500
0
(b)
166°30'E
167°E
167°30'E
0
17.5
35
degree
N
10 km
77°30'S

Fig. 10

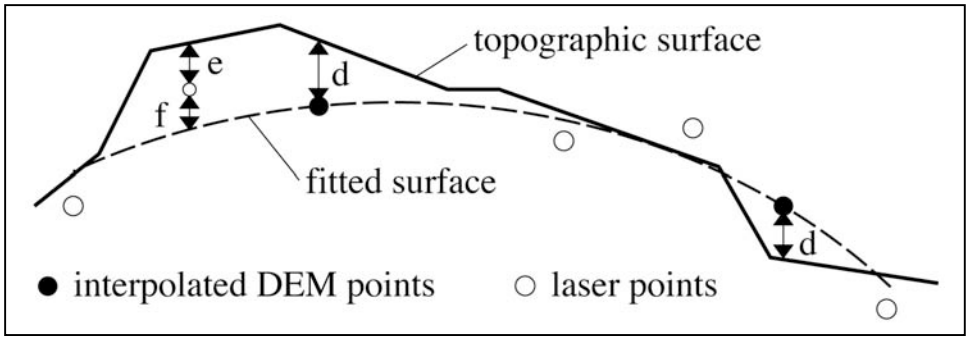
topographic surface
e
d
f
fitted surface
d
interpolated DEM points
laser points

Fig. 11

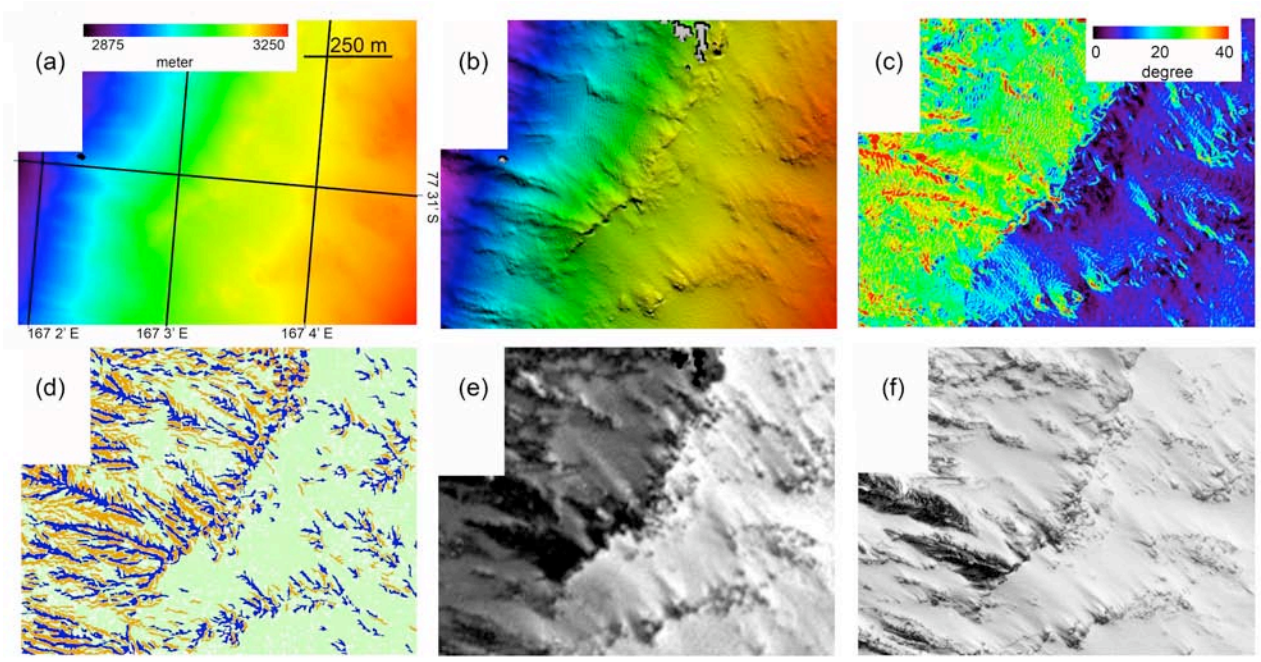
(a)
2875
3250
meter
250 m
(b)
(c)
0
20
40
degree
77 31' S
167 2' E
167 3' E
167 4' E
(d)
(e)
(f)

Fig.12

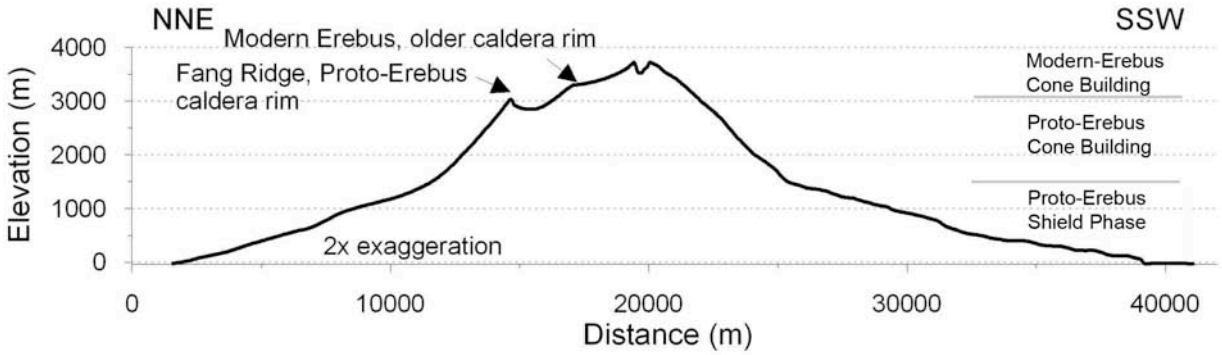
NNE
SSW
Modern Erebus, older caldera rim
Fang Ridge, Proto-Erebus caldera rim
Modern-Erebus Cone Building
Proto-Erebus Cone Building
Proto-Erebus Shield Phase
2x exaggeration
Elevation (m)
4000
3000
2000
1000
0
0
10000
20000
30000
40000
Distance (m)

Fig. 13

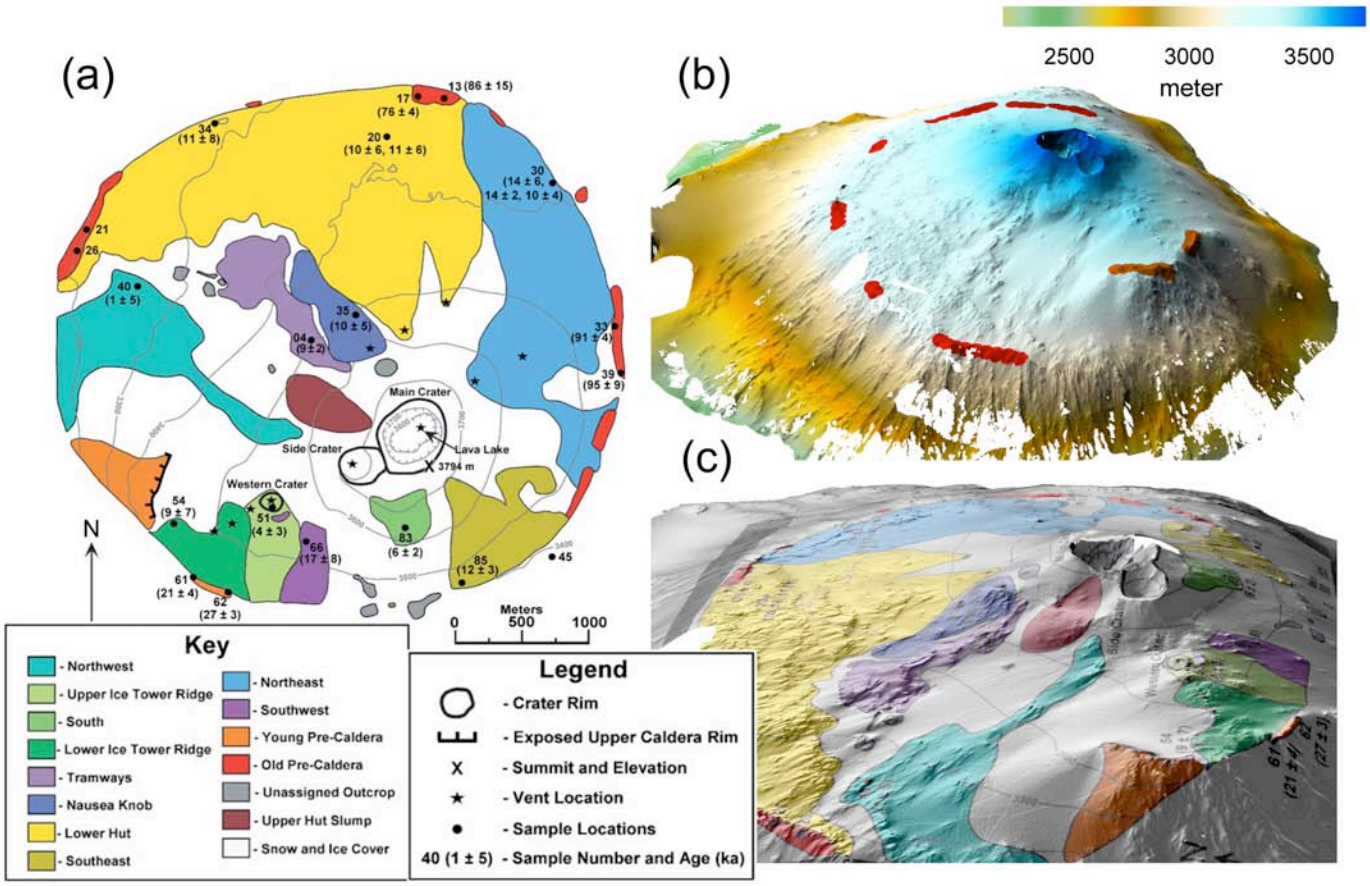
(a)
(b)
(c)
2500
3000
3500
meter
Main Crater
Side Crater
Lava Lake
3794 m
Western Crater
N
Meters
0
500
1000
Key
- Northwest
- Upper Ice Tower Ridge
- South
- Lower Ice Tower Ridge
- Tramways
- Nausea Knob
- Lower Hut
- Southeast
- Northeast
- Southwest
- Young Pre-Caldera
- Old Pre-Caldera
- Unassigned Outcrop
- Upper Hut Slump
- Snow and Ice Cover
Legend
- Crater Rim
- Exposed Upper Caldera Rim
X - Summit and Elevation
- Vent Location
- Sample Locations
40 (1 ± 5) - Sample Number and Age (ka)

Fig. 14

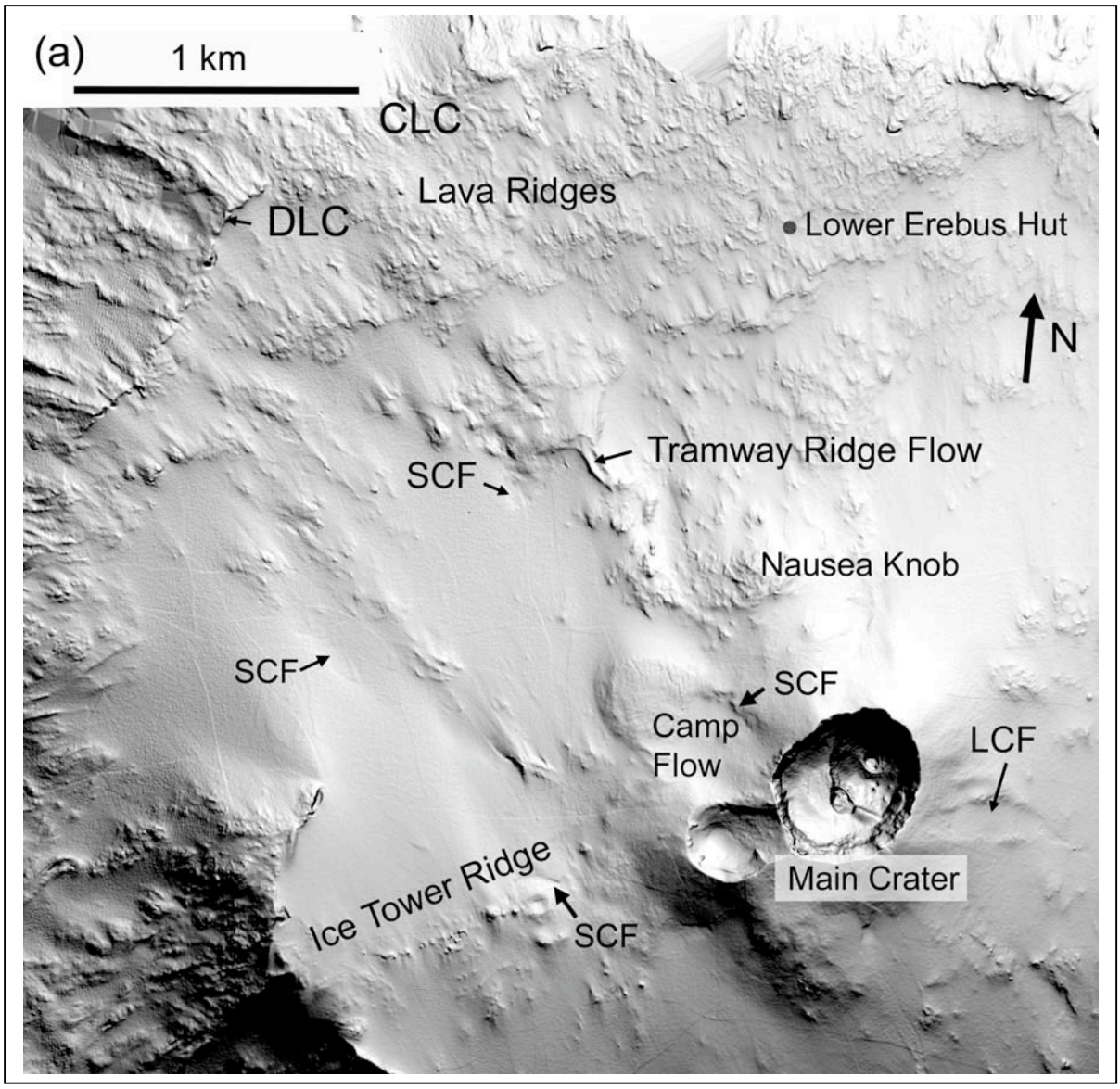
(a)
1 km
CLC
Lava Ridges
DLC
Lower Erebus Hut
N
Tramway Ridge Flow
SCF
Nausea Knob
SCF
SCF
Camp
Flow
LCF
Main Crater
Ice Tower Ridge
SCF

Fig. 14

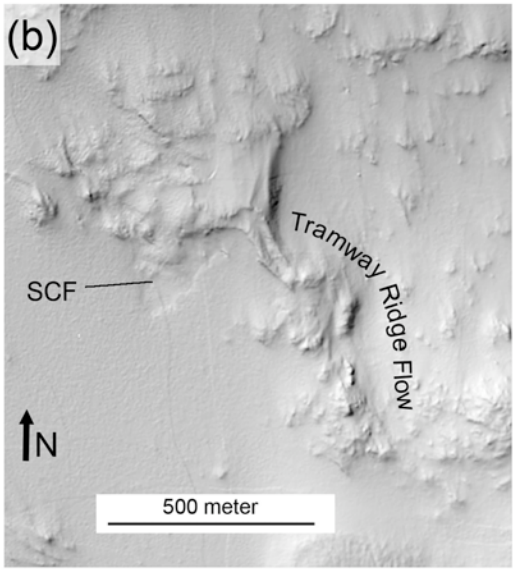

Fig. 15

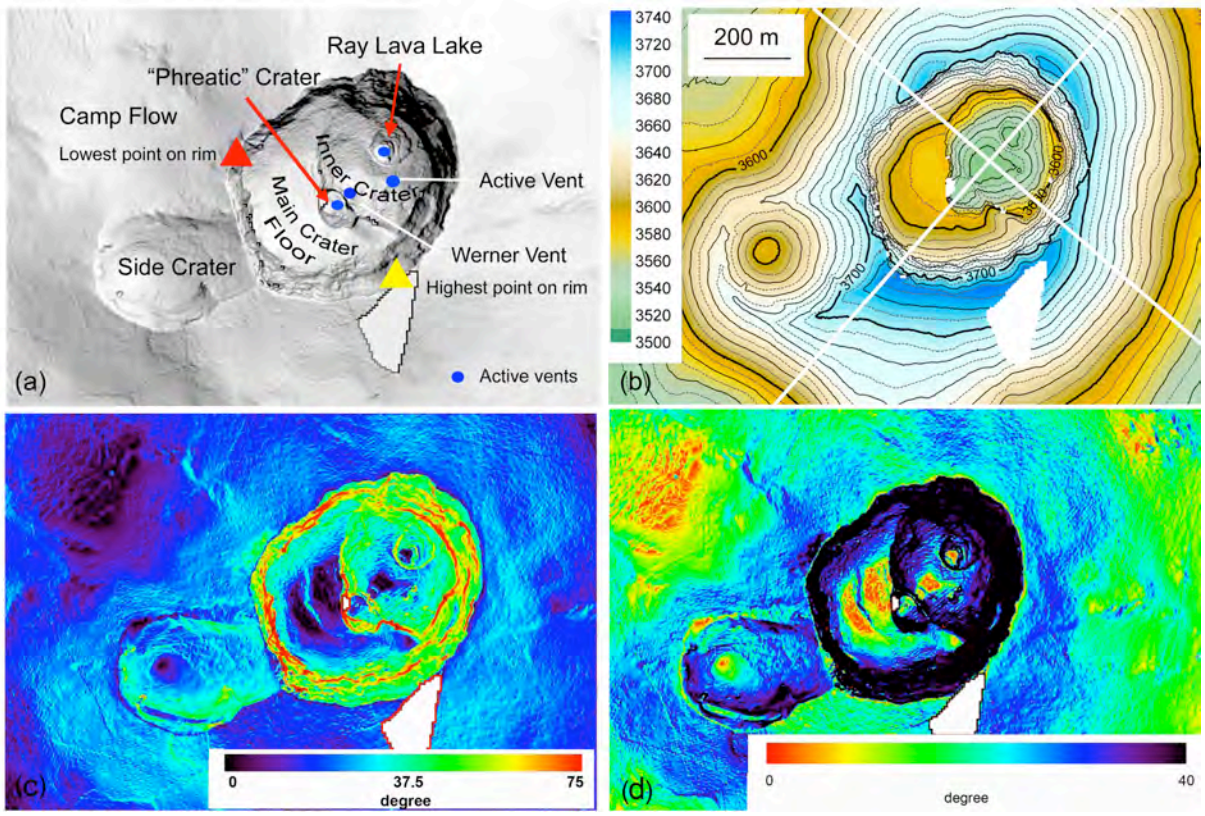
Ray Lava Lake
"Phreatic" Crater
Camp Flow
Lowest point on rim
Inner Crater
Active Vent
Main Crater Floor
Side Crater
Werner Vent
Highest point on rim
Active vents
(a)
3740
3720
3700
3680
3660
3640
3620
3600
3580
3560
3540
3520
3500
200 m
3600
3700
(b)
0
37.5
75
degree
(c)
0
40
degree
(d)

Fig. 16

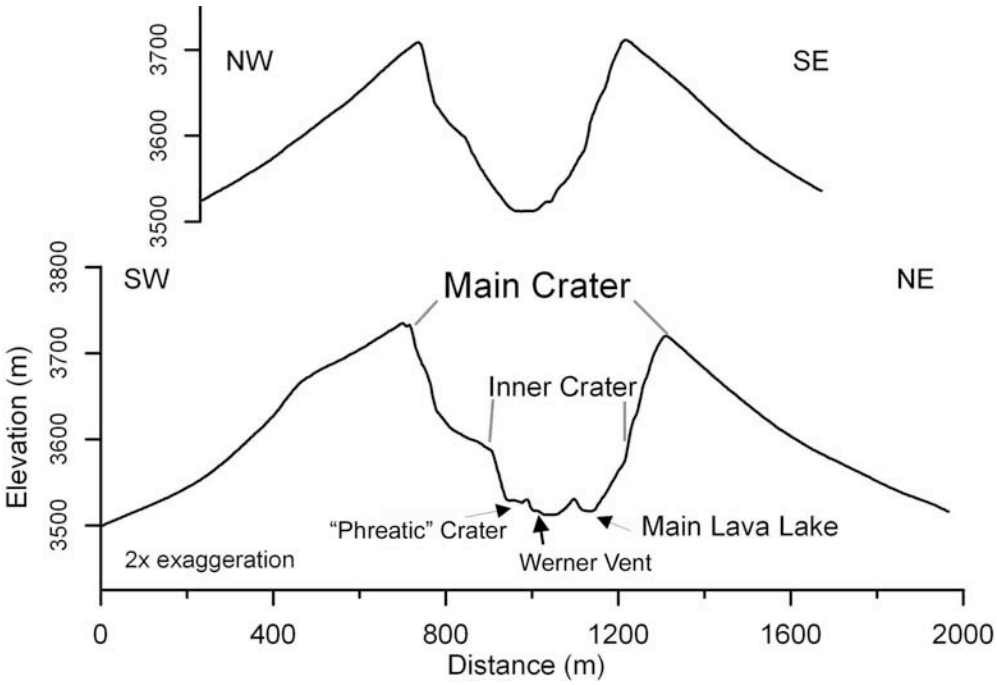
NW
SE
3700
3600
3500
SW
NE
Main Crater
Inner Crater
"Phreatic" Crater
Main Lava Lake
Werner Vent
2x exaggeration
Elevation (m)
3800
3700
3600
3500
0
400
800
1200
1600
2000
Distance (m)

Fig. 17

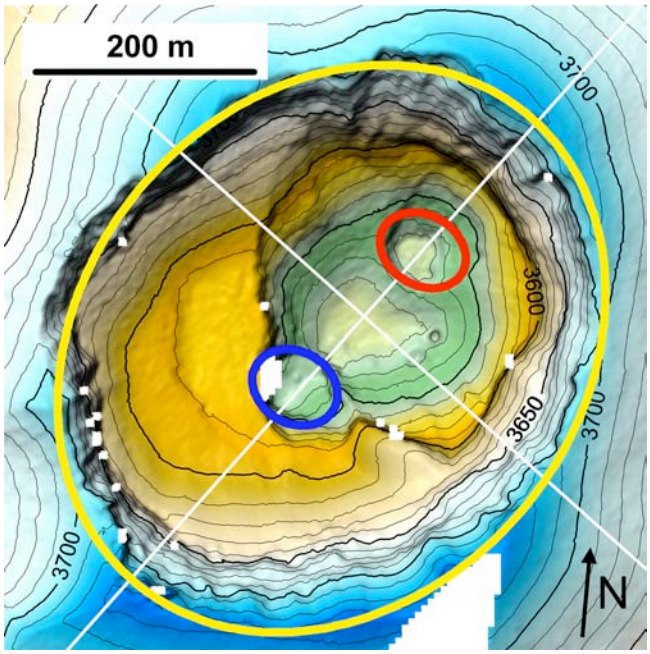

Fig. 18

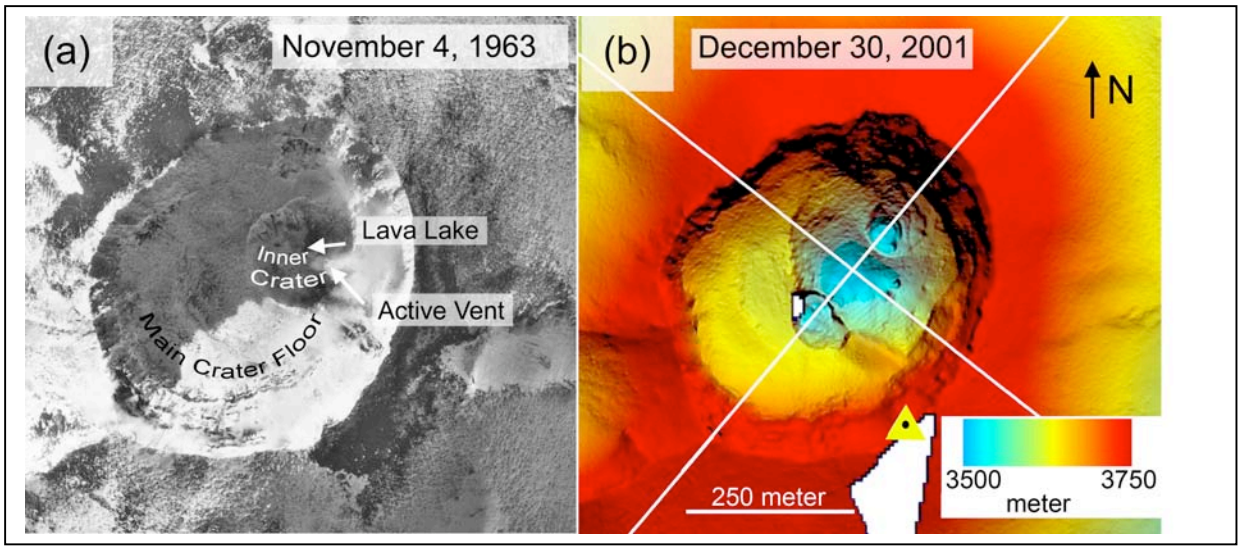
(a)
November 4, 1963
Lava Lake
Inner Crater
Active Vent
Main Crater Floor
(b)
December 30, 2001
N
250 meter
3500
3750
meter

Fig. 19

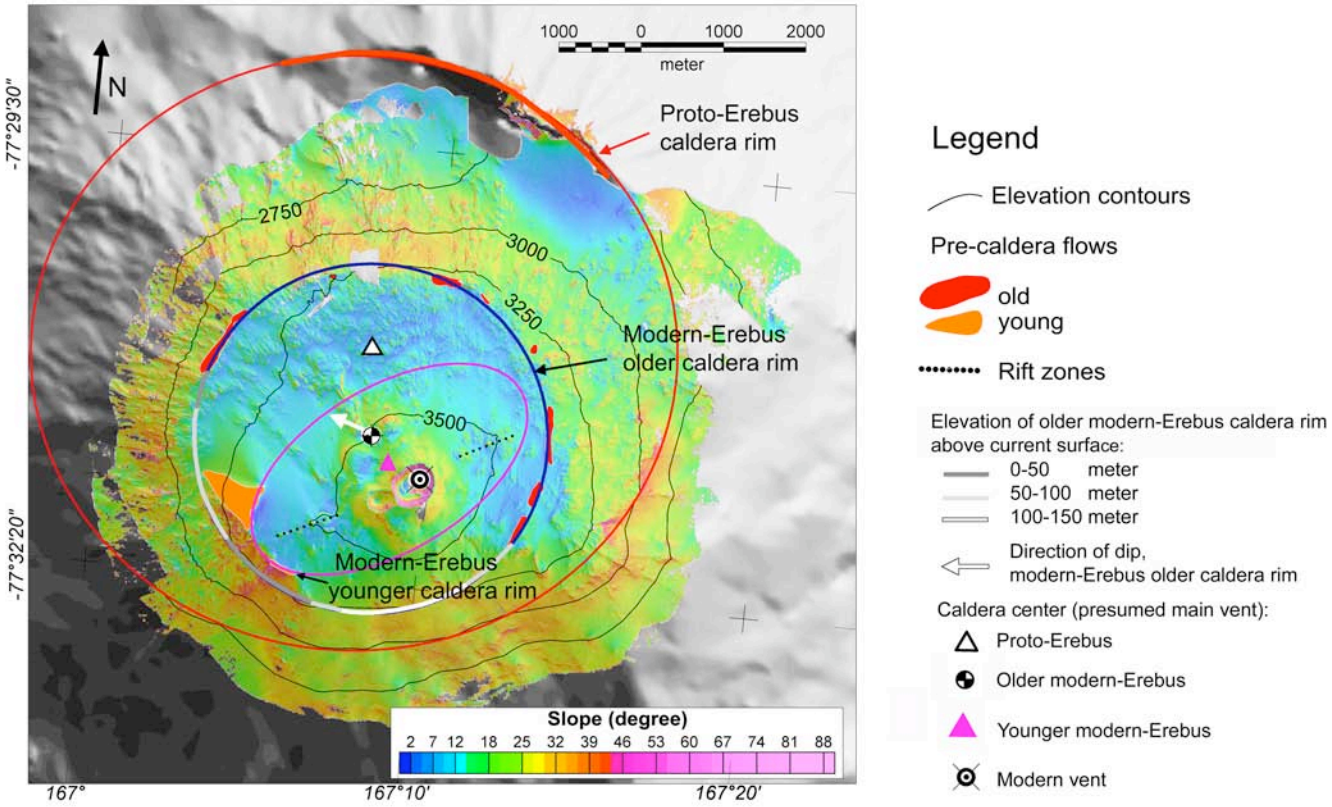
1000 0 1000 2000
meter
N
Proto-Erebus
caldera rim
2750
3000
3250
3500
Modern-Erebus
older caldera rim
Modern-Erebus
younger caldera rim
Slope (degree)
2 7 12 18 25 32 39 46 53 60 67 74 81 88
-77°29'30"
-77°32'20"
167°
167°10'
167°20'
Legend
Elevation contours
Pre-caldera flows
old
young
Rift zones
Elevation of older modern-Erebus caldera rim above current surface:
0-50 meter
50-100 meter
100-150 meter
Direction of dip, modern-Erebus older caldera rim
Caldera center (presumed main vent):
Proto-Erebus
Older modern-Erebus
Younger modern-Erebus
Modern vent

Fig. 20

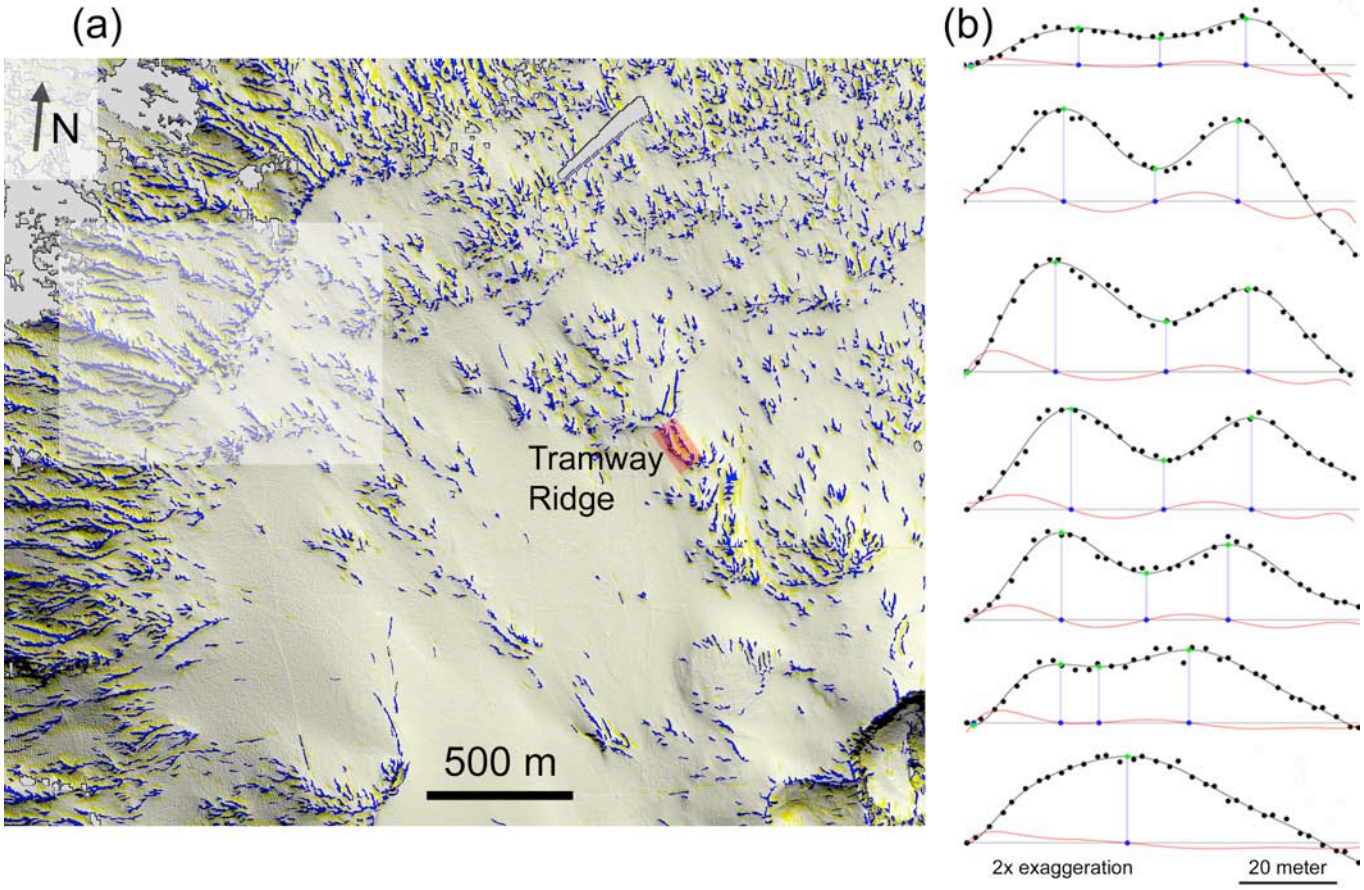

Fig. 21

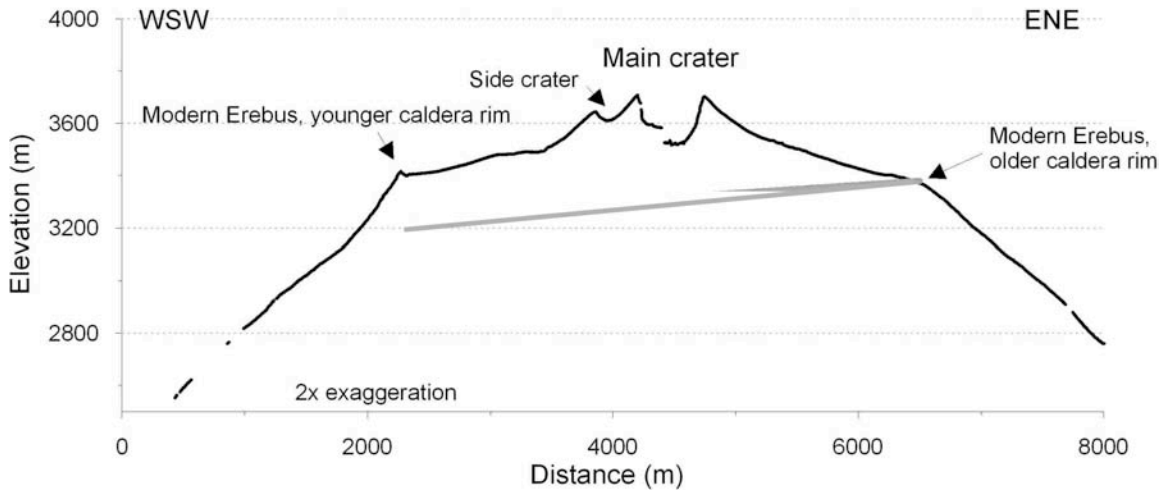
4000
3600
3200
2800
Elevation (m)
WSW
ENE
Main crater
Side crater
Modern Erebus, younger caldera rim
Modern Erebus,
older caldera rim
2x exaggeration
0
2000
4000
6000
8000
Distance (m)